Chandra X-ray Grating Spectrometry of η Carinae near X-ray Minimum: I. Variability of the Sulfur and Silicon Emission Lines

D. B. Henley[1], M. F. Corcoran[2,3], J. M. Pittard[4], I. R. Stevens[5], K. Hamaguchi[2,3], and T. R. Gull[6]

ABSTRACT

We report on variations in important X-ray emission lines in a series of *Chandra* grating spectra of the supermassive colliding wind binary star η Car, including key phases around the X-ray minimum/periastron passage in 2003.5. The X-rays arise from the collision of the slow, dense wind of η Car with the fast, low-density wind of an otherwise hidden companion star. The X-ray emission lines provide the only direct measure of the flow dynamics of the companion's wind along the wind-wind collision zone. We concentrate here on the silicon and sulfur lines, which are the strongest and best resolved lines in the X-ray spectra. Most of the line profiles can be adequately fit with symmetric Gaussians with little significant skewness. Both the silicon and sulfur lines show significant velocity shifts and correlated increases in line widths through the observations. The $\mathcal{R}$ = forbidden-to-intercombination ratio from the Si XIII and S XV triplets is near or above the low-density limit in all observations, suggesting that the line-forming region is > 1.6 stellar radii from the companion star, and that the emitting plasma may be in a non-equilibrium state. We show that simple geometrical models cannot simultaneously fit both the observed centroid variations and changes in line width as a function of phase. We show that the observed profiles can be fitted with synthetic profiles with a reasonable model of the emissivity along the wind-wind collision boundary. We use this analysis to help constrain the line formation region as a function of orbital phase, and the orbital geometry.

Subject headings: X-rays: stars –stars: early-type–stars: individual (η Car)

[1]Department of Physics and Astronomy, University of Georgia, Athens, GA 30602; dbh@physast.uga.edu

[2]NASA Goddard Space Flight Center, CRESST, Astrophysics Science Division, Code 662, Greenbelt, MD 20771

[3]Universities Space Research Association, 10211 Wincopin Circle, Columbia, MD 21044

[4]School of Physics and Astronomy, University of Leeds, Woodhouse Lane, Leeds, LS2 9JT, U.K.

[5]School of Physics and Astronomy, University of Birmingham, Edgbaston, Birmingham, B15 2TT, U.K.

[6]Astrophysics Science Division, Code 667, Goddard Space Flight Center, Greenbelt, MD 20771

1. INTRODUCTION

The supermassive star η Car (Davidson & Humphreys 1997) is notorious for its extraordinarily large luminosity and its implicitly large mass ($L > 4 \times 10^6 L_\odot$ and $M \sim 100 M_\odot$, Hillier et al. 2001), the beautiful bipolar "Homunculus" nebula which shrouds it (Gaviola 1950), its wild instability (most notably the "Great Eruption" of 1843 which created the Homunculus) and its continued broad-band variations (Sterken et al. 1996; Davidson et al. 1999). Understanding η Car is important for a wide variety of astrophysical topics regarding the formation and evolution of extremely massive stars, the processes by which such stars lose mass and angular momentum, and the ways in which they interact with their surroundings.

η Car exhibits variability over a wide range of wavelengths, from radio (Duncan & White 2003), through infrared (Whitelock et al. 1994, 2004; Damineli 1996; Damineli et al. 1997, 2000; Davidson et al. 2000), optical (Steiner & Damineli 2004), and ultraviolet (Smith et al. 2004) to X-rays (Ishibashi et al. 1999; Corcoran 2005). All these variations have a characteristic cycle of almost exactly 2024 days, which strongly suggests that η Car is a long period ($P = 2024$ day) binary (Damineli 1996; Damineli et al. 1997). The observed variability is believed to result (directly or indirectly) from the interaction of the fast wind ($v_c \sim 3000$ km s^{-1}) and ionizing radiation from the companion with the dense, slow wind of the Luminous Blue Variable (LBV) primary ($v_\eta \sim 500$ km s^{-1}). In this scheme, the X-rays are produced by the collision of the two stars' winds, which causes the companion's fast wind to be shock-heated to tens of MK (Pittard et al. 1998; Pittard & Corcoran 2002). The high temperature of the shocked wind of the companion explains the hard X-rays ($kT \gtrsim 4$ keV) first directly associated with the star by *Einstein* (Seward et al. 1979). Similar hard X-ray emission is seen from WR 140, the "canonical" long period eccentric massive colliding wind binary (Pollock et al. 2005).

Our understanding of the system has become more sophisticated due in part to dense multiwavelength monitoring near the times of the X-ray eclipses in 1998 and 2003.5. These observations showed that, at the same time that the X-ray brightness of the source reaches minimum, the ionization state of the circumstellar medium rapidly decreases (Duncan et al. 1995; Nielsen et al. 2007), the infrared (Whitelock et al. 2004) and millimeter-wave (Abraham et al. 2005b) brightness of the source also drops, absorption components in excited He I P-Cygni emission lines undergo rapid blue-to-red velocity shifts (Nielsen et al. 2007), He II 4686-Å emission (Steiner & Damineli 2004; Martin et al. 2006) appears, shows a similar blue-to-red centroid shift, then disappears, and the far UV flux from η Car drops rapidly (Iping et al. 2005). In all colliding wind models these changes (which last only about 90 days of the 2024-day cycle) occur near periastron passage, and require a high eccentricity ($e \sim 0.9$). However, important details regarding the nature of the wind-wind collision are

still not well constrained; there is still debate concerning, for example, whether the X-ray minimum occurs near inferior conjunction (when the companion is in front of the LBV primary) or superior conjunction; the magnitude of the companion's wind velocity; and the mass loss rates from either star. These uncertainties limit our understanding of how the companion star affects the system, and, ultimately limit our knowledge of the evolutionary state of the system.

The detailed analysis of excited He I P-Cygni absorption lines in spatially resolved spectra by Nielsen et al. (2007) showed radial velocity variations which mimic the orbital radial velocity variations expected in an eccentric ($e \approx 0.9$) binary system with the semi-major axis pointed towards the observer (longitude of periastron $\omega \sim 270°$) and an assumed inclination $i \approx 41°$. These spectral variations suggest that the ionized helium zone in the wind of the cool, massive primary star approaches the observer prior to periastron passage. They also showed that the velocity amplitude of the He I P-Cygni absorption components $\sim 140 \, \mathrm{km \, s^{-1}}$, was larger than expected if the absorption arises in the dense wind of the more massive star. They concluded that the velocity variations are probably strongly influenced by ionization effects due to the interaction of the companion star's photospheric UV radiation with the wind of the cool primary star. They also suggested that some of the He I emission might originate within or near the wind-wind collision and thus could be a diagnostic of that collision. However the complex influence of the companion's radiation with the primary wind makes interpretation of such diagnostics far from straightforward.

X-ray line profiles provide the most direct probe of the dynamics of the wind of the unseen companion after it is shock-heated in the wind-wind interaction, since these lines originate in the high temperature plasma near the wind-wind shock interface. X-ray lines directly reflect the dynamic properties of this hot shocked gas. In this paper we present our analysis of the high resolution X-ray grating spectra of η Car obtained by the High Energy Transmission Grating Spectrometer (HETGS; Markert et al. 1994) on the *Chandra* X-ray Observatory (Weisskopf et al. 2002) obtained as part of a large observing campaign around the time of the 2003.5 X-ray minimum. A preliminary analysis of these data has appeared in Henley (2005).

In this paper we discuss our analysis of spectra in the energy range near 2 keV obtained by the Medium and High Energy Gratings (MEG and HEG). This energy range is dominated by line emission from Si and S hydrogen-like and helium-like ions. These lines form in the cooler regions of the shocked gas farther along the wind-wind collision zone, and thus provide a better measure of the flow dynamics of the shock-heated wind of the companion along the colliding wind interface than the iron lines, which originate near the hottest part of the shock near the stagnation point where flow velocities are low. In this energy range the HETGS

first order spectra has sufficient resolution to resolve the component lines of the He-like triplets providing useful density and temperature diagnostics. Unfortunately, potentially crucial line emission from C, N, and O (which could be used to measure abundances of the shocked companion's wind and help constrain the evolutionary state of the companion) are not observable in the central source due to the heavy absorption by the cold gas and dust in the Homunculus.

This paper is organized as follows. The observations and the data reduction are described in §2, and the HETGS silicon and sulfur emission lines are discussed in §3. In §4 we apply a simple geometrical model of the wind-wind collision to the variations in line centroids and widths. In §5 we apply synthetic colliding wind line profiles to the observed HETGS silicon and sulfur profiles. We discuss the results of the emission line analysis in §6, and our conclusions are presented in §7. Throughout this paper we quote 1σ errors.

2. OBSERVATION DETAILS AND DATA REDUCTION

The details of the six *Chandra* HETGS observations of η Car are given in Table 1. For the purposes of this paper we designate the observations with CXO, subscripted with the date in YYMMDD format (cf. Hamaguchi et al. 2007). The earliest observation was in 2000 November (CXO_{001119}; Corcoran et al. 2001b; Pittard & Corcoran 2002), approximately half-way between the previous X-ray minimum in late 1997 and the X-ray minimum in mid-2003. The second observation was taken approximately one year later (2002 October; CXO_{021016}), by which time the X-ray flux had increased by a factor of ~2. The four remaining observations were taken over the space of approximately five months around the X-ray minimum which occurred, as expected, in late 2003 June. In particular, they approximately correspond to X-ray maximum (2003 May; CXO_{030502}), the early part of the descent to X-ray minimum (2003 June; CXO_{030616}), the X-ray minimum itself (2003 July; CXO_{030720}), and the recovery from the minimum (2003 September; CXO_{030926}). All data were read out using the Advanced Camera for Imaging Spectroscopy spectroscopic array (ACIS-S). The outer ACIS-S CCD chips (S0 and S5) were switched off, and we used a reduced read-out window in order to reduce pileup. This truncates the low-energy spectra but results in little real data loss since the stellar source is heavily absorbed. The spectra at energies $E \lesssim 3$ keV obtained during and just after the X-ray minimum (CXO_{030720} and CXO_{030926}) are contaminated by the "Central Constant Emission" (CCE) component identified by Hamaguchi et al. (2007) from *XMM-Newton* observations taken during the 2003 X-ray minimum. This means that the silicon and sulfur lines from these two spectra do not accurately reflect the emission from the colliding wind plasma alone (with the exception of S XVI in CXO_{030926}, which is

not as badly contaminated). However, for completeness, we include measurements of the line properties for all six observations, including CXO_{030720} and CXO_{030926}, in our discussion in §§3 and 4.

The data for all six observations were reduced from the Level 1 events files using CIAO[1] v3.4 and CALDB v3.3.0.1. These versions are much improved over the earlier versions used by Corcoran et al. (2001b) and Henley (2005). We followed the threads available from the *Chandra* website[2]. We first removed the `acis_detect_afterglow` correction, and generated a new bad pixel file using `acis_run_hotpix`. We then reprocessed the Level 1 events file with the latest calibration using `acis_process_events`. This applies a new ACIS gain map, the time-dependent ACIS gain correction, the ACIS charge transfer inefficiency (CTI) correction, and pixel and PHA randomization. We then used `tgdetect` to determine the position of the zeroth-order image of η Car, `tg_create_mask` to determine the location of the HEG and MEG "arms", and `tg_resolve_events` to assign the measured events to the different spectral orders. After applying grade filters (*ASCA* grades 0, 2, 3, 4, and 6 were kept) and good time intervals, we used `destreak` to remove streaks caused by a flaw in the serial readout which randomly deposits significant amounts of charge along the pixel row as charge is read out. Finally, we used `tgextract` to extract the grating spectra from the events file. Spectral response files were also generated following the *Chandra* threads: we generated redistribution matrix files (RMFs) and ancillary response files (ARFs) using `mkgrmf` and `fullgarf`, respectively.

The *Chandra* HETGS spectra of η Car for each of the six *Chandra* observations are shown in Figures 1 through 6. For each observation, the $+1$ and -1 orders of each grating (HEG and MEG) have been co-added, and the spectra have been binned up to 0.01 Å, except for the observation taking during the X-ray minimum (CXO_{030720}; Fig. 5), which has been binned up to 0.02 Å. Note that the spectra are shown with the same y-axis range, except for CXO_{030720}.

With the exception of CXO_{030720}, which is the faintest spectrum by an order of magnitude, the spectra all exhibit prominent continuum emission and numerous emission lines. Particularly prominent are forbidden-intercombination-resonance (f-i-r) triplets from He-like Fe XXV ($\lambda_{resonance} = 1.85$ Å), S XV ($\lambda_{res} = 5.04$ Å) and Si XIII ($\lambda_{res} = 6.65$ Å), Lyα emission from H-like S XVI ($\lambda = 4.73$ Å) and Si XIV ($\lambda = 6.18$ Å), and K-shell fluorescent emission from cool Fe ($\lambda = 1.94$ Å). Other lines which are visible (not necessarily in all spectra) include Ca XX at 3.0 Å, Ca XIX at 3.2 Å, Ar XVIII at 3.7 Å, Ar XVII + S XVI at 4.0 Å, Si XIV

at 5.2 Å, and Si XIII at 5.7 Å. The Fe K lines will be discussed elsewhere (Paper II; M. F. Corcoran et al., in preparation). Here we concentrate on the brightest of the lower-excitation lines: the H-like Lyα line and He-like f-i-r triplet from Si and S. Although line shifts and widths can be measured for some of the other lines, the four lines that we concentrate on here are the only ones for which results can be obtained from all six observations. Furthermore, the analysis of these weaker lines is consistent with the analysis of the stronger lines presented here (for more detailed discussion of these weaker lines see Henley 2005).

3. SILICON AND SULFUR LINE PROFILES

3.1. Gaussian Modeling

We analyzed the *Chandra* spectra of η Car using unbinned, non-co-added spectra, so no spectral information was lost. Because some bins contain low numbers of counts, the Cash statistic (Cash 1979) was used instead of the χ^2 statistic. To measure each emission line's properties, we analyzed each line (or multiplet) individually over a narrow range of wavelengths encompassing just the line of interest. We then fit a model to the data comprising a power-law continuum component plus Gaussian components to model the line emission. The number of Gaussians used, and how their parameters are tied together, depended on the nature of the line being analyzed (Pollock et al. 2005; Henley et al. 2005). For the Lyα lines (which are closely spaced doublets, separated by $\approx$5 mÅ), we used two Gaussians. The Doppler shifts of the two components were constrained to be equal, as were their widths, and the intensity of the longer-wavelength component was constrained to be half that of the shorter-wavelength component. The He-like f-i-r triplets were fit with three Gaussians, the Doppler shifts and widths of which were tied together as for the Lyman lines, but the amplitudes of which were allowed to vary. For the intercombination line we used the rest wavelength of the $2\,^3P_1 \to 1\,^1S_0$ transition, and ignored the fainter $2\,^3P_2 \to 1\,^1S_0$ transition.

The analysis described here was carried out using SHERPA, as distributed with CIAO v3.4. The data were not background subtracted, as the Cash statistic cannot be used on background-subtracted data, nor was the background separately modeled out. This is not a problem because for the lines of interest the background count rate is more than an order of magnitude lower than the source count rate in the relevant energy range. Furthermore, the background spectra show no prominent spectral features, so any background contribution would be included in the continuum component used in the fitting.

Our procedure for a given line from a given observation was to fit the same model to all four spectra (HEG $\pm$1, MEG $\pm$1) simultaneously. We then assessed goodness-of-fit using a

Monte Carlo method (as the Cash statistic by itself gives no goodness of fit information), using a similar method to that of Helsdon & Ponman (2000). The best-fit model was used to simulate 1000 synthetic emission lines. Poisson noise was added to each simulated line, and then each was compared with the original model to calculate its Cash statistic. Hence, for a given emission line model, we obtained the distribution of Cash statistic values expected for datasets generated from that model. By comparing the observed Cash statistic with this distribution, we determined the probability that the model could have produced the observed data. In practice we did this by measuring the mean and standard deviation (σ) of the simulated Cash statistic values – if the observed Cash statistic lay more than 2σ away from the mean, the fit was regarded as "poor".

We found that, when fitting to all four spectra simultaneously, Gaussian profiles gave acceptable fits to most of the lines. A visual inspection of the poorer fits indicated that the lines in different orders were sometimes slightly offset from each other in wavelength. This may be due to uncertainty in the determination of the centroid position of the zeroth-order image on the ACIS-S detector – if the determined position were offset from the true position, the wavelengths in the $+1$ and -1 orders would be offset in opposite directions. To overcome this, where possible we fit the model to the four spectra individually, and then averaged the results. For some fainter lines (the sulfur lines in CXO_{001119}, and the lines in CXO_{030720} and CXO_{030926}) we were unable to constrain the model in all four individual spectra. In these cases, we adopted the results obtained by fitting all four spectra simultaneously. For the Si XIII triplet in CXO_{030720}, even this did not work, and instead we obtained our results by fitting just to the MEG $+1$ and -1 spectra.

The emission line shifts, widths, fluxes, and equivalent widths measured from this Gaussian modeling are given in Table 2. The rest wavelengths are adopted from ATOMDB[3] v1.3.1. Table 3 shows the results in Table 2 expressed as velocities. Figures 7 and 8 show the Si XIII and Si XIV lines from the four brightest spectra (CXO_{001119}, CXO_{021016}, CXO_{030502}, and CXO_{030616}), along with the best-fitting Gaussian line model. The models were fit to each spectral order individually, which is why in several cases the Gaussians are offset in the different orders.

Figure 9 shows the measured line shifts and widths plotted against phase ϕ (see Table 1), where $\phi = 1$ corresponds to the start of the X-ray minimum in 2003 June (Corcoran 2005). We have not corrected for the systemic velocity of η Car (-8 km s^{-1}; Smith 2004), as it is negligible compared with the measurement errors. The general trend of the line shifts is that the lines have small blueshifts of $\sim$100 km s^{-1} away from the X-ray minimum (CXO_{001119}

---

[3]http://cxc.harvard.edu/atomdb

and CXO_{021016}), the blueshifts increase to ~300-700 km s^{-1} just before the X-ray minimum (CXO_{030502} and CXO_{030616}; note that the lines in CXO_{030616} are generally more blueshifted than in CXO_{030502}), and the blueshifts return to ~100 km s^{-1} after the start of X-ray minimum (CXO_{030720} and CXO_{030926}). The exception to this is S XVI which is slightly redshifted in the last two observations. The general trend of the line widths is that they increase from ~800 km s^{-1} (FWHM) away from the X-ray minimum to ~1400 km s^{-1} just before the start of minimum, and then return to ~800 km s^{-1} afterward. However, as noted in §2, the last two observations (being much fainter than the previous ones) are contaminated by the CCE component (Hamaguchi et al. 2007) at wavelengths longward of about 4Å. As a result of this contamination, the shifts and widths determined from the silicon and sulfur lines in these two spectra do not accurately reflect the kinematics of the wind-wind collision (with the exception of S XVI in CXO_{030926}, which is not as badly contaminated).

The connection between the variation in the line shifts and the variation in the line widths is further illustrated in Figure 10. There is a clear correlation between shift and width, with the broader lines being more blueshifted. For these data, Spearman's rank correlation coefficient is −0.58, and Kendall's τ statistic is −0.47 (Press et al. 1992). Both of these statistics show that correlation is significant at the 1% level.

Figure 11 shows the variation in the emission line fluxes, plotted with the 2–10 keV *RXTE* lightcurve (Corcoran 2005). For S XV and Si XIII we plot the resonance line flux. As expected, the variation in the line fluxes generally follows that of the broadband emission. However, not all the lines' fluxes vary in the same way – for example, the Si XIII flux does not rise as much as the Si XIV flux in the first three observations, which in turn does not rise as much as the S XVI flux. These differences between the lines are shown more clearly in Figure 12, which shows the ratios of the line fluxes to the contemporaneous 2–10 keV flux measured with *RXTE* (Corcoran 2005). The ratios are normalized to the values from CXO_{001119}. From CXO_{001119} to CXO_{021016} ($\phi = 0.528$ to 0.872), the emission lines stay fairly constant with respect to the broadband flux (the S XVI and Si XIV lines actually brighten slightly). However, just before the X-ray minimum (CXO_{030502} and CXO_{030616}; $\phi = 0.970$ and 0.992) the lines grow fainter with respect to the broadband flux. This is what one would expect as the amount of absorption starts increasing: the emission lines in the ~2–3 keV range will be more strongly attenuated than the broadband flux over the whole 2–10 keV band. Furthermore, one would expect the longer wavelength lines to show this effect the most. From Figure 12 one can see that in CXO_{030502} this effect is weakest for the S XVI line and strongest for the Si XIII resonance line. Rather surprisingly, however, the Si XIV line is less affected than the S XV resonance line. Furthermore, the S XV resonance line brightens slightly with respect to the broadband flux between CXO_{030502} and CXO_{030616}. Note in the final observation, after the recovery (CXO_{030926}; $\phi = 1.043$), that the lines are very faint

with respect to the broadband flux. This is because absorption is still having a strong effect on the spectrum, and the observed 2–10 keV flux is coming from shorter wavelengths than the Si and S lines (one can see from Fig. 6 that most of the flux in CXO$_{030926}$ is shortward of 4 Å).

3.2. Line Shapes

Behar et al. (2007) co-added Lyα, He-like resonance and He-like forbidden lines of Si, S, and Ar and showed that the resulting profile exhibits a significant asymmetry on the blueward side of the line. They find that the lines develop blue wings extending to $\sim$2000 km s^{-1} in CXO$_{030502}$ and CXO$_{030616}$, and attribute this to the development of a jet with line-of-sight velocity $\sim$−2000 km s^{-1} near periastron. We also looked for evidence of profile asymmetries, using the individual (i.e., non-co-added) lines in each observation. A visual inspection of Figures 7 and 8 suggests that some of the lines may indeed be asymmetric. We find that some of the lines have negative skewness in wavelength (or velocity) space, i.e., an extended tail on the blue side of the line. For example, the Si XIV line is skewed in this way in CXO$_{021016}$ and CXO$_{030502}$ (except in the HEG +1 spectrum). However, the observed asymmetry is not as apparent in the Si XIII triplet, which makes it difficult to determine whether this apparent asymmetry is real. We noted that Gaussians give good fits to the individual observed lines. A Gaussian profile would give a bad fit to a strongly skewed line.

In order to quantify the amount of asymmetry in the observed line profiles, we calculated the skewness of the distribution of photon wavelengths that make up a given observed line. The skewness S is given by (Press et al. 1992)

$$S = \frac{1}{N\sigma_\lambda^3} \sum_{i=1}^{N} (\lambda_i - \bar{\lambda})^3, \tag{1}$$

where N is the number of photons, λ_i is the wavelengths of the ith photon, and $\bar{\lambda}$ and σ_λ are the sample mean and standard deviation of the wavelengths. If our null hypothesis is that the underlying wavelength distribution is Gaussian, the standard deviation of S is approximately $\sqrt{6/N}$ (Press et al. 1992). In the HETGS spectra, the photons are in bins of width 2.5 mÅ (HEG) and 5 mÅ (MEG). When estimating S, we assume that all the photons in a given bin have a wavelength equal to the bin's central wavelength. We do not take into account the contribution of the continuum, but for most observations this should not affect the results too badly, as the lines are much brighter than the continuum.

We looked for skewness in the Lyα lines of S XVI and Si XIV, and the resonance and forbidden lines of Si XIII. We did not include the resonance and forbidden lines of S XV,

as the S XV intercombination line is more prominent (see below), which could affect the results. In particular we looked for cases where $|S| > 3\sqrt{6}/N$, although it should be noted that this might not be a strong enough criterion for deciding if the skewness in the line is significant[4]. We examine the individual HEG and MEG +1 and −1 orders, and also the co-added first-order HEG and MEG spectra (to increase the signal-to-noise ratio).

We found that the Si XIV Lyα and Si XIII resonance lines are significantly negatively skewed in CXO$_{030502}$ and CXO$_{030616}$, but the evidence is less convincing for the forbidden line in these observations (it is significantly skewed in the MEG +1 order, but not in the other orders). The S XVI Lyα line is not significantly skewed in these observations (see Fig. 13, which compares the HEG −1 profiles of S XVI and Si XIV Lyα from CXO$_{030502}$). For the other observations, there is no strong evidence for line skewing – in a few cases a line might exhibit skewing in one spectral order, but not in the other three.

Although some of the lines seem to be skewed, visual inspection of Figures 7 and 8 suggests that these asymmetries are relatively modest. Detailed modeling of these line profile asymmetries reveal finer details of the wind-wind collision (see §5), but the Gaussian-fitting results should provide sufficiently accurate information on the gross structure of the wind-wind collision.

We note that, when comparing the results of fitting individual lines from individual orders, the lines are sometimes slightly offset, possibly due to a slight inaccuracy in the position of the zeroth-order image. Also, when the lines are analyzed individually, we find that different ions sometimes yield different shifts and widths (see Fig. 9). This suggests that adding the profiles from different lines and different spectral orders in order to improve the signal-to-noise (Behar et al. 2007) might not yield accurate profiles.

3.3. The $\mathcal{R}$ Ratios of the He-Like Triplets

The ratio of the forbidden (f) and intercombination (i) line intensities of a helium-like ion, $\mathcal{R} = f/i$, can often provide useful information on the conditions in and location of the emitting plasma. This is because the metastable upper level of the forbidden line can be depopulated to the upper level of the intercombination line by UV photoexcitation or electron collisions: increasing the UV flux or the electron density reduces $\mathcal{R}$ from its low-density, low-UV limit $\mathcal{R}_0$. In the case of a hot star possessing a stellar wind, where both

---

[4]Press et al. (1992) caution that "it is good practice to believe in skewnesses only when they are several or many times as large as [the standard deviation]."

electron density and UV flux vary as $1/r^2$, $\mathcal{R} < \mathcal{R}_0$ implies that the line-emitting region is close to the stellar photosphere.

In Table 4 we present the $\mathcal{R}$ ratios for Si XIII and S XV measured from each of our HETGS spectra. Also in the table we present $\mathcal{R}_0$, calculated by Blumenthal et al. (1972) at the temperature at which the triplet has its maximum emissivity (8.9 MK for Si XIII and 14.1 MK for S XV), and the UV transition wavelengths to go from the upper level of the forbidden line to the upper levels of the intercombination lines. In all observations, the Si XIII $\mathcal{R}$ ratio is greater than $\mathcal{R}_0$, implying that the forbidden line is enhanced with respect to the intercombination line. This has been observed for O VII in the *XMM-Newton* RGS spectrum of the supernova remnant N132D (Behar et al. 2001), and for several different ions in the *Chandra* HETGS spectrum of the WR+O binary WR 140 (Pollock et al. 2005). However, before we discuss the implications of these large $\mathcal{R}$ ratios, we first discuss the reliability and statistical significance of these measurements.

It is possible that too high a continuum level would lead to line fluxes that are systematically too low. The weak intercombination line would be most severely affected, and this would lead to an artificially high $\mathcal{R}$ ratio. We have investigated whether or not this is the case in our analysis by adjusting the range of wavelengths we include when fitting to the Si XIII triplet. The results in Table 2 were obtained by fitting to the spectra between 6.4 and 7.0 Å (note that the plots in Figure 7 do not show this full wavelength range). When we use a narrower range of wavelengths, the forbidden and intercombination fluxes tend to be smaller. While none of the individual decreases is statistically significant, the fact that there is a systematic shift suggests that with the narrower wavelength range the line fluxes are systematically underestimated. However, we do not see the opposite effect when we increase the wavelength range from 6.4–7.0 Å. The amounts by which the fluxes change are much smaller than when we decreased the wavelength range, and there is no systematic shift in one direction (i.e., some fluxes increase slightly, and some decrease slightly). Furthermore, from a visual inspection of the fits, there is no evidence that a power-law is not a good fit to the continuum over the range of wavelengths that we use. From these observations, we conclude that our large $\mathcal{R}$ ratios are not due to an inaccurate continuum level.

Because of the rather large errors on $\mathcal{R}$, only the $\mathcal{R}$ ratios for CXO_{021016} and CXO_{030502} differ by more than 2σ from $\mathcal{R}_0$, and no observed $\mathcal{R}$ ratio differs by more than 3σ from $\mathcal{R}_0$. However, if we take as the null hypothesis that $\mathcal{R} = \mathcal{R}_0$ for all six of our observations, this gives $\chi^2 = 18.35$ for 6 degrees of freedom (χ^2 probability = 0.54%). This implies that $\mathcal{R}$ is different from $\mathcal{R}_0$ for at least some of our spectra.

If $\mathcal{R}$ is genuinely larger than $\mathcal{R}_0$ in our *Chandra* spectra, this may be evidence of inner-shell ionization of Li-like Si to He-like Si ($1s^2 2s + e^- \rightarrow 1s2s + 2e^-$), which leads to an enhanced

forbidden line. This in turns suggests non-equilibrium conditions; specifically, an ionizing plasma. This is because inner-shell ionization requires both a high electron temperature and an abundance of Li-like ions, two conditions which tend not to hold simultaneously in an equilibrium plasma (Mewe & Schrijver 1978). In the following section we present further evidence of non-equilibrium conditions, based on the $G = (f + i)/r$ ratio (here r refers to the resonance line). An alternative explanation is that our measured $\mathcal{R}$ ratios indicate that the temperature of the line-forming region is significantly different from the temperature of maximum emissivity at which $\mathcal{R}_0$ is calculated.

For S xv the values of $\mathcal{R}$ are generally close to $\mathcal{R}_0$, which suggests inner-shell ionization might not be as important for this ion as it is for Si xiii. In an equilibrium plasma, $\mathcal{R}$ can be used to place constraints on the electron density n_e and the UV flux, and hence place constraints on the location of the X-ray–emitting plasma. One can express $\mathcal{R}$ as a function of n_e and the photoexcitation rate ϕ to go from the upper level of the forbidden line to the upper level of the intercombination line:

$$\mathcal{R} = \frac{\mathcal{R}_0}{1 + (\phi/\phi_C) + (n_e/n_C)}, \tag{2}$$

where ϕ_C and n_C are quantities dependent only on atomic parameters and the electron temperature (Blumenthal et al. 1972). The ratio $\mathcal{R}$ tends toward the limit $\mathcal{R}_0$ when $\phi \ll \phi_C$ and $n_e \ll n_C$. Blumenthal et al. (1972) give $n_C = 1.9 \times 10^{14}$ cm^{-3} and $\phi_C = 9.16 \times 10^5$ s^{-1} for S xv at the temperature of maximum emissivity. If we assume $\dot{M}_c = 10^{-5}$ $M_\odot$ yr^{-1} and $v_c = 3000$ km s^{-1} for the companion (Pittard & Corcoran 2002), we find that $n_e \ll n_C$ everywhere in the companion's wind; unless the shock compression ratio is very large (several hundred or more), this will also be true in the wind-wind collision region. Thus, electron collisions are not expected to affect the $\mathcal{R}$ ratio.

Blumenthal et al. (1972) also tabulate $\phi_\star/\phi_C$, where $\phi_\star$ is the photoexcitation rate on the surface of a 10^5-K blackbody. We estimate $\phi_\star/\phi_C$ for η Car's companion by scaling the Blumenthal et al. (1972) value for S xv, assuming the companion is a blackbody with $T = 36,000$ K (this is in the middle of the range of effective temperatures given by Verner et al. 2005). We obtain $\phi_\star/\phi_C = 1.6$, which means that on the surface of the companion we have $\mathcal{R} = \mathcal{R}_0/(1 + 1.6) = 0.77$, with $\mathcal{R}$ increasing toward $\mathcal{R}_0$ as we move away from the star. Unfortunately, the fact that $\mathcal{R}$ is fairly large even on the surface of the companion, and the large errors on $\mathcal{R}$ in Table 4, make it difficult to place strong constraints on the location of the emitting plasma. As one moves away from the companion, the photoexcitation rate decreases as $\phi(r)/\phi_C = 2W(r)\phi_\star/\phi_C$, where $W(r) = 0.5[1 - \sqrt{1 - (r_c/r)^2}]$ is the geometrical dilution factor, and r is the distance from the center of the companion, whose radius is r_c. Note that r_c is not well known, though Ishibashi et al. (1999) estimate $r_c \sim 50R_\odot$. If we

take the result for CXO_{001119}, and say that the measurements imply $\mathcal{R} > 1.7$ (i.e., the 1σ lower limit), this gives $r > 1.6r_c$ for the location of the X-ray–emitting plasma.

The low S XV $\mathcal{R}$ ratio for CXO_{021016} seems to suggest that the S XV emission originates close to the companion in that observation. If we were to take $\mathcal{R} < 1.5$, this would imply $r < 1.2r_c$. However, closer inspection of the spectra shows that the S XV intercombination line is noticeably brighter in the HEG -1 spectrum than in the HEG $+1$ spectrum. This can be seen in Figure 14, which shows the S XV triplet from the CXO_{021016} HEG spectra, along with the S XV triplet from the CXO_{030502} HEG spectra for comparison. The $\mathcal{R}$ ratios for CXO_{021016} from the individual HEG orders are 0.6 ± 0.2 (-1) and 1.9 ± 1.1 ($+1$), while the $\mathcal{R}$ ratio obtained from the HEG $+1$ fit results combined with those from the two MEG orders is 1.8 ± 0.5. It therefore seems that the low $\mathcal{R}$ ratio for CXO_{021016} is mainly due to the bright intercombination line in the HEG -1 spectrum. We have examined the first-order HEG image, using the CIAO tool `tg scale reg` to establish the position of the S XV intercombination line. We find that there is no detector feature (such as a hot pixel) or X-ray source which is contaminating the intercombination line in the HEG -1 spectrum. We have also compared the forbidden and intercombination line fluxes measured in the $+1$ and -1 orders of both gratings for each observation. We have done this for Si XIII and S XV. In principle, this would be a total of 48 comparisons (6 observations $\times$ 2 gratings $\times$ 2 ions $\times$ 2 lines). However, as we cannot fit to individual orders in all cases, in practice we find we can only make 30 such comparisons. Among these comparisons, only the CXO_{021016} S XV intercombination line measured by the HEG differs by more than 2σ between the $+1$ and -1 orders (the difference is 2.2σ). With the null hypothesis that the line flux is the same for both orders, the probability of such a large difference is 2.8%. Therefore, it is not surprising that, among our set of 30 $+1/-1$ comparisons, we find one case where the two values differ by 2.2σ. This suggests that the large intercombination line flux in the CXO_{021016} HEG -1 spectrum is a statistical fluke, and that there is no convincing evidence that the S XV $\mathcal{R}$ ratio for this observation really is significantly lower than those in the other observations.

As a final point, it should be noted that the spectral type of the companion is not known, and a 36,000-K blackbody may poorly represent its UV flux at the wavelengths relevant to the above analysis. A more detailed model of its spectrum is required to place more accurate constraints on the location of the X-ray–emitting plasma.

3.4. The G Ratios of the He-Like Triplets

We also measured the $G = (f + i)/r$ line ratios for the helium-like Si XIII and S XV triplets. The G ratio decreases with temperature. It is also sensitive to densities for

$n > 10^{12}$ cm^{-3}, which is well above the range of densities expected in the wind-wind collision in η Car from hydrodynamical simulations ($< 10^{11}$ cm^{-3}; see for example Pittard & Corcoran 2002). The measured G ratios are given in Table 5, and are plotted in Figure 15. Also plotted in this figures is the temperature dependence of the G ratios based from the Astrophysical Plasma Emission Database (APED; Smith et al. 2001), version 1.3.1, along with the temperature range derived by Hamaguchi et al. (2007) from fitting the *XMM-Newton* X-ray spectrum in the 2–10 keV band for data outside the X-ray minimum with collisional equilibrium models. The measured G ratios suggest temperatures of $T < 8 \times 10^6$ K for Si XIII and $T < 13 \times 10^6$K for S XV which are much lower than the range in temperature derived by Hamaguchi et al. (2007), 40×10^6 K $< T < 64 \times 10^6$ K. The G ratio we measure for the Si XIII triplet, $0.56 < G < 1.31$ is consistent with the G ratio derived for γ^2 Vel, another colliding wind binary, by Henley et al. (2005). The analysis by Pollock et al. (2005) of the pre-periastron spectrum of WR 140, like η Car a long period, eccentric colliding wind binary with a characteristic X-ray temperature of ~ 4 keV ($\sim 50 \times 10^6$ K), yields $G = 0.72 \pm 0.07$ for the Si XIII triplet and $G = 0.97 \pm 0.17$ for the S XV triplet, again similar to the values we derive for these lines in η Car and implying a temperature of only a few million K. This again is some evidence that the X-ray emitting plasma in η Car is not in collisional equilibrium.

4. A SIMPLE GEOMETRICAL MODEL OF THE COLLIDING WIND REGION

It is clear from the preceding section that η Car's X-ray emission lines show variability around the time of the X-ray minimum. We first attempt to understand this variability in terms of a simple geometrical characterization of the emission region as a conical surface of constant opening angle. This analysis has been applied to features in optical emission lines from WR 79 to constrain orbital and other parameters of the system (Lührs 1997), and also to X-ray emission lines from WR 140 (Pollock et al. 2005) and γ^2 Velorum (Henley et al. 2005).

4.1. Description of the Model

We assume that the X-ray emission comes from a conical emission region with opening half-angle β, whose symmetry axis lies along the line of centers with the apex pointing toward the primary star, and along which material streams at speed v_0. The viewing angle γ is the angle between the line of centers and the line of sight. The geometry is illustrated in Figure 16. Assuming that there is no azimuthal velocity component, the centroid shift ($\bar{v}$)

and velocity range $(v_{max} - v_{min})$ of an emission line are given by (Lührs 1997; Pollock et al. 2005; Henley et al. 2005)

$$\bar{v} = -v_0 \cos\beta \cos\gamma, \tag{3}$$

$$v_{max} - v_{min} = 2\Delta v = 2v_0 \sin\beta \sin\gamma. \tag{4}$$

The viewing angle γ can be calculated from the orbital solution. We first define Ψ as the angle between the line of centers at the time being considered and the line of centers when the companion star is in front; Ψ can be calculated from the true anomaly Φ and the longitude of periastron ω:

$$\cos\Psi = \cos(\Phi + \omega - 90°). \tag{5}$$

If i is the orbital inclination, then γ is given by

$$\cos\gamma = \cos\Psi \sin i. \tag{6}$$

When comparing the predictions of this model with the observed data, $\bar{v}$ may simply be equated to the shifts in Table 3. The relation between Δv and the measured Gaussian line widths is less straightforward. We assume that the observed velocities range from $v_{min} \approx$ (Shift) $-$ (FWHM) to $v_{max} \approx$ (Shift) $+$ (FWHM), and proceed by simply equating Δv in equation (4) to the observed FWHM.

The orbital parameters we assume initially are given in Table 6, which are largely based upon Corcoran et al.'s (2001a) analysis of the *RXTE* light curve, with a revised period from Corcoran (2005). Note that the time of periastron passage T_0 in Table 6 is actually the time of the start of the X-ray minimum (Corcoran 2005), which was used to calculate the phases in Table 1. However, as periastron is expected to occur near the time of the X-ray minimum, assuming the two times are equal has little effect on the results. If the time of periastron passage is allowed to differ from the time of the start of the X-ray minimum, this will only result in the curves calculated below being shifted slightly to the left or right. The orbit specified by the parameters in Table 6 is shown in Figure 17. The length scale of the orbit is set by assuming masses of $80M_\odot$ and $30M_\odot$ for the primary and the companion, respectively (Corcoran et al. 2001a). However, the scale of the orbit is not important for our analysis – all that matters is how the viewing angle varies with time.

In addition to the orbital elements, we also need to assume an opening angle β for the wind-wind interaction region, and a speed v_0 for material streaming along the cone. From hydrodynamical simulations of the wind-wind collision in η Car, we adopt a shock opening half-angle $\beta = 58°$ (Henley 2005). This is consistent with the shock opening angle estimated from the equivalent width of the Fe fluorescence line measured with *XMM-Newton*

(Hamaguchi et al. 2007). At large distances from the line of centers, the velocity along the shock cone v_0 tends toward the terminal velocity of the companion star's wind (3000 km s^{-1}). However, the observed emission lines are likely to originate from nearer to the line of centers (Henley et al. 2003) – the outer regions are not favored for X-ray line emission because (a) the gas number density n falls off with distance from the line of centers (and the line luminosity scales as n^2) and (b) the gas temperature also falls off, reducing the populations of H- and He-like ions whose lines we are discussing here. However, very near the line of centers (where v_0 is much lower), the gas is too hot for most of the observed ions to exist in significant amounts, and so the line emission falls off here too despite the greatly increased density. Using the line profile model described in Henley et al. (2003), we find that most of the line emission should originate where $v_0 \approx 2000$–3000 km s^{-1}.

The solid red line in Figure 18 shows the results of the geometrical model compared to the observed line shifts and widths. The observed variation in the line widths is in qualitative agreement with the model in that the widths increase around $\phi = 1$ and decrease again afterward, although the model parameters we have used predict larger widths than are observed. However, the agreement between the observed and model velocity shifts is poor using the model parameters adopted above: away from the X-ray minimum, the model predicts large blueshifts of $\sim$800 km s^{-1}, whereas we observe much smaller blueshifts of $\sim$100 km s^{-1}, while near X-ray minimum, the model predicts redshifted lines, in contrast to the increasing blueshifts which we observe. Some of this discrepancy may be due to the assumed values of the shock parameters and orbital elements. We consider the dependence of the model velocities and widths on the parameters v_0, β, i, ω and e below.

4.2. Dependence on the Shock Parameters

The model line centroids and widths depend on the conditions assumed for the boundary surface of the idealized wind-wind interaction, namely the flow speed v_0 and the cone opening angle β. Since the flow speed v_0 appears as a multiplicative constant in equations (3) and (4), varying v_0 simply varies the amplitude of the variation in the predicted shifts and widths. For example, lowering v_0 by a few hundred km s^{-1} would bring the predicted widths into better agreement with the observed widths. However, the discrepancy between the predicted and observed shifts would still exist.

From inspection of equations (3) and (4), one can see that varying β will also change the amplitude of the variation in the predicted shifts and widths. In particular, increasing β decreases the amplitude of the velocity shift and increases the amplitude of the variation in line width. However, if everything else is kept the same, the model still predicts redshifted

lines around the time of the X-ray minimum, instead of the observed blueshifted lines.

4.3. Dependence on the Orbital Elements

Varying the inclination i varies the amplitude of the variation in the viewing angle γ. In an edge-on binary ($i = 90°$), γ varies from 0° at one conjunction[5], to 90° at quadrature, to 180° at the other conjunction, and back again to 0°. In contrast, a face-on binary ($i = 0°$) is always observed at $\gamma = 90°$. In general, γ varies between $90° - i$ and $90° + i$ during the course of the orbit. The result of this is that varying the inclination i also varies the amplitude of the shift and width variations. Maximum variability occurs when $i = 90°$, and there is no variability for $i = 0°$. However, whereas reducing v_0 or β reduces the predicted widths as well as the amplitude of the variation, as i tends to 0° the width tends to $v_0 \sin \beta$ rather than to zero (see eq. [4]). We find that simply varying the inclination cannot bring the model into good agreement with the observations.

We also considered the effect of changing the orbital eccentricity. Increasing the eccentricity means that the viewing angle changes more rapidly during periastron passage. This in turn means that the predicted shifts and widths will change more rapidly. As a result, the peak at $\phi = 1$ in the solid red curve in Figure 18(a) and the double-peaked feature at $\phi = 1$ in the solid red curve in Figure 18(b) both become narrower with increasing eccentricity, and broader with decreasing eccentricity. This is shown by the dashed red curves in Figure 18.

Finally, varying the longitude of periastron ω has the largest effect on determining the phase dependence of the velocities in the model. The solid blue curves in Figure 18 show a model with $\omega = 185°$, which means that the orbit has been rotated 90° clockwise. In this orientation the semimajor axis is approximately perpendicular to the line of sight, and the companion passes in front of the primary just before periastron. One can see that this ω does yield lines with small shifts away from $\phi = 1$, and with increasing blueshifts as ϕ approaches 1. However, the increase in the model blueshift occurs too soon in phase compared with the observed centroid shifts. Increasing the eccentricity helps by delaying the blueshift in phase, and by making the change in centroid velocity more rapid near periastron passage. The blue dashed curve in Figure 18(a) shows a model in which $\omega = 185°$ and $e = 0.95$ instead of 0.9. Although the agreement is not formally acceptable, this model is in rough qualitative agreement with the variation in the line shifts prior to the X-ray minimum, though it fails to describe the observed variations in line widths. Further adjustment of e, ω, and v_o or β might further improve the agreement.

---

[5]Depending on which star has the more powerful wind.

After the X-ray minimum, the new model predicts lines redshifted by a few hundred km s^{-1}, whereas the observed lines generally have small ($\sim$100 km s^{-1}) blueshifts. As noted in §2, the silicon and sulfur lines are significantly contaminated by emission from the CCE component in the last two *Chandra* spectra (except for S XVI in CXO$_{030926}$). This means that these lines do not accurately reflect the centroids of the lines produced by the wind-wind collision. However, with this new value of ω the agreement between the predicted and observed widths shown in Figure 18(b) is poorer than it was for the original model: away from the X-ray minimum the new model predicts larger widths than are observed, and the predicted widths decrease around $\phi = 1$, instead of increasing.

In summary, we have shown how adjusting the various parameters in our geometrical model for the line shifts and widths affects the model predictions. We find that by adjusting certain parameters it is possible to bring the model into rough qualitative agreement with the observations for a subset of the shifts or widths, but we have not found a set of parameters which describes both the line shifts and variations in line widths simultaneously in all of the observations well, though admittedly we have not carried out a complete exploration of the whole parameter space. However, by seeing how the individual model parameters affect the model curves it is not easy to see which combination of parameters would bring this simple geometrical model into good agreement with the observations.

5. SYNTHETIC LINE PROFILE MODELING

In the previous section we showed that there is poor agreement between the shifts and widths predicted by the simple geometrical model, and those that are observed in the HETGS spectra of η Car. With a longitude of periastron $\omega \approx 270°$, we can get reasonable agreement with the observed variation of the widths, and with $\omega \approx 180°$ we can get reasonable agreement with the observed variation of the shifts. However, we cannot match the variation of both simultaneously. Furthermore, when the axis of shock cone is nearly perpendicular to the line of sight (i.e., $\gamma \approx 90°$), the above-described model predicts broad double-peaked line profiles (with the peaks at $\sim \pm v_0 \sin \beta$). With the orbital parameters discussed above, we expect at least one of our observations to have $\gamma \approx 90°$. However, we do not see double-peaked profiles in any of our spectra. To address these issues, we have developed a more sophisticated model for calculating emission line profiles, taking into account both the shape of the wind-wind collision region and the variation in the speed at which material flows away from the stagnation point. Falceta-Gonçalves et al. (2006) showed that a similar detailed line profile model, including turbulent broadening and intrinsic absorption was needed to fit the phase-dependent, asymmetric C III 5696 Å line from the WR+O colliding wind binary

Br22.

5.1. Description of the Model

We calculate the shape of the wind-wind collision region using the results of Cantó et al. (1996), who have derived equations for the surface of momentum balance between two colliding spherical winds. This model is for two totally radiative winds with complete mixing between them. While this is not expected to be the case in η Car, it provides a useful starting point for modeling the line emission, in particular for determining the shape of the surface of momentum balance. We assume that the X-ray–emitting region is optically and spatially thin, and coincident with the surface of momentum balance. The shape of the wind-wind collision surface depends on the wind momentum ratio $\eta = \dot{M}_c v_c / \dot{M}_\eta v_\eta$, and the flow speed along the surface also depends on the wind speeds of the stars v_c and v_η. For our canonical model we adopt $\eta = 0.2$, $v_c = 3000$ km s^{-1} and $v_\eta = 500$ km s^{-1} (Pittard & Corcoran 2002). The resulting shape of the wind-wind collision surface is shown in Figure 19.

Using the Cantó et al. (1996) equations, we find that the flow speed along the wind-wind collision surface away from the stagnation point tends toward ~ 900 km s^{-1} far from the stagnation point. However, hydrodynamical simulations suggest that the flow speed in the X-ray–emitting region tends toward the wind speed of the companion (i.e., ~ 3000 km s^{-1}). To allow for this, we introduce a velocity scaling factor f_v, by which we multiply the Cantó et al. flow speeds before calculating the line profile. This scaling factor is a free parameter in the fitting described in the following section.

We assume that the wind-wind interaction surface is cylindrically symmetric about the line of centers. Therefore, at each point along the wind-wind interaction the emission profile is that of an expanding ring. This ring of material flows along the wind-wind collision surface at speed $v_t = f_v v_{C96}$, where v_{C96} is the local flow speed given by the Cantó et al. (1996) equations. Locally, the flow velocity makes an angle $\beta_{\rm local}$ with the line of centers, as illustrated in Figure 20. Note that this is the local shock cone opening angle, as opposed to asymptotic value which we used in §4. We assume that each infinitesimal portion of this ring emits a Dirac δ function line profile, shifted according to the line-of-sight velocity v. The emission profile $\epsilon(v)$ of the whole ring is then

$$\epsilon(v) \propto \left[v_t^2 \sin^2 \beta_{\rm local} \sin^2 \gamma - (v + v_t \cos \beta_{\rm local} \cos \gamma)^2 \right]^{-1/2} \tag{7}$$

where γ is the viewing angle, defined as before as the angle between the line of sight and the line of centers (see Figs. 16 and 20). Note that $\epsilon(v)$ goes to infinity at $v_{\rm min} = v_t(-\sin \beta_{\rm local} \sin \gamma - cos \beta_{\rm local} \cos \gamma)$ and $v_{\rm max} = v_t(\sin \beta_{\rm local} \sin \gamma - cos \beta_{\rm local} \cos \gamma)$; $\epsilon(v)$ is un-

defined outside those velocities. The function $\epsilon(v)$ goes to infinity because we assume that the intrinsic line profile produced at each point on the ring is a Dirac δ function. In reality, the intrinsic line profile produced at each point on the ring will be broadened; we take this into account in our calculations by convolving the line profile calculated using equation (7) with a Gaussian (see below). Note also that the integral of $\epsilon(v)$ from v_{min} to v_{max} is finite, and is equal to the line luminosity of the expanding ring.

Using this model we cannot calculate the line emissivity at different points along the wind-wind collision surface self-consistently (unlike, say, the X-ray line model based upon hdyrodynamical simulations described in Henley et al. 2003). Instead, we adopt a simple formula for calculating the line luminosity as a function of the distance x measured along the wind-wind collision surface from the stagnation point. The line luminosity $l(x)$ per unit distance x is given by

$$l(x) = \frac{4}{\pi^{1/2} x_{\mathrm{peak}}^3} L_{\mathrm{line}} x^2 \mathrm{e}^{-(x/x_{\mathrm{peak}})^2}, \qquad (8)$$

where x_{peak} is the value of x at which $l(x)$ peaks and L_{line} is the total line luminosity, although in this model we are only interested in the line *shapes*, so L_{line} is irrelevant. The form of equation (8) was chosen after some experimenting with fitting simple functions to the curves in Fig. 2 of Henley et al. (2003). The function $l(x)$ encompasses variations in the temperature, the density, and the emitting volume per unit x. Some examples of $l(x)$ are plotted in Figure 19. Note that mixing with cooler material and/or non-equilibrium ionization may affect the form of equation (8), but such effects are beyond the scope of the present modeling.

Our model line profiles are calculated by summing the individual expanding-ring profiles from each point along the wind-wind collision surface, weighted by the function $l(x)$. We convolve this summed profile with a Gaussian with FWHM = 100 km s^{-1} to model thermal broadening. The resulting profile is then folded through the HETGS response for comparison to the observed profiles, as described below.

5.2. Comparison to the Observed Profiles

The comparison to the observed profiles was carried out using XSPEC[6] v11.3.2. We generated a grid of profiles with γ = 5°, 10°, 15°, ..., 175°, f_v = 1, 1.25, 1.5, ..., 5, and x_{peak} = 0.1, 0.2, 0.4, ..., 6.4. We converted the profiles from velocity space to energy space

---

[6]http://heasarc.gsfc.nasa.gov/docs/xanadu/xspec/

using the rest energy of the line we wished to analyze, and used the grid of resulting profiles to generate an XSPEC table model[7].

In our analysis we concentrated first on the Si XIV Lyα line, as the velocity resolution is higher at its wavelength than at that of the S XVI Lyα line, and there are no problems with confusion with nearby lines, unlike the He-like f-i-r triplets. Our initial approach was to fit the model profiles to the observed lines with γ, f_v and x_{peak} all as free parameters. We also added a power-law component to model the continuum, and for a given observation we fit the model to all four unbinned spectral orders (HEG ± 1, MEG ± 1) simultaneously, using the C statistic (a modified form of the Cash [1979] statistic, which is implemented in XSPEC). We applied the model to the first four HETGS observations (CXO$_{001119}$, CXO$_{021016}$, CXO$_{030502}$, and CXO$_{030616}$), as the last two (CXO$_{030720}$ and CXO$_{030926}$) are contaminated by the CCE component as discussed above.

The best-fitting viewing angles we obtained were similar for all four observations we analyzed: $\approx 34°$ for CXO$_{001119}$, $\approx 22°$ for CXO$_{021016}$ and CXO$_{030502}$, and $\approx 14°$ for CXO$_{030616}$. This is surprising, given the large range of phases over which the observations were taken (for example, the phase changed by ≈ 0.1 between CXO$_{021016}$ and CXO$_{030502}$, yet the best-fitting viewing angles for these two observations differ by $\approx 0.1°$). We could not find an orbital solution (specified by ω, i, and e) which matched the best-fitting viewing angles for all four observations.

We therefore tried a slightly different approach, by trying to find an orbital solution which would give model line profiles consistent with the observed profiles for all observations. We fixed $e = 0.95$, and for a few sample values of ω and i we generated theoretical line profiles and compared them to the observations, allowing x_{peak} and f_v to vary until the C statistic was minimized. We constrained f_v to be the same for all four observations we investigated. Figure 21 shows these best-fit line profiles for $\omega = 270°$ (green) and $\omega = 180°$ (blue), with $i = 50°$ in each case. These values of ω and i are similar to the values published by Corcoran et al. (2001a) and Smith et al. (2004), respectively. They are also similar to the values discussed in §4. As shown in Figure 21, these values of ω and i result in profiles which have too much emission redward of the Si XIV line center. This is especially true for models in which $\omega = 180°$ and $i = 50°$. The $\omega = 270°$, $i = 50°$ models do a reasonable job in matching the Si XIV, except for the last observation just before the start of the X-ray minimum (CXO$_{030616}$). We then attempted to see if we could generate a reasonable fit to all the observed profiles for some value of ω and i. After some experimentation, we found that a model with $\omega = 210°$ and $i = 70°$ yielded profiles that provided reasonable descriptions

---

[7]http://xspec.gsfc.nasa.gov/docs/xanadu/xspec/xspec11/manual/node61.html

of the shapes of the Si XIV lines in all the observations. These profiles are shown in red in Figure 21. The orbit of η Car with $e = 0.95$ and $\omega = 210°$ is shown in Figure 22 (cf. Fig. 17). The best-fitting values of f_v and x_{peak} are shown in the upper part of Table 7. The x_{peak} values imply that the Si XIV emission originates further from the stagnation point (relative to the stellar separation) in the later two observations, as x_{peak} is ~8 times larger for these observations. The fact that x_{peak} is larger just before periastron than at apastron means that at periastron the Si XIV emission originates from a region with much higher flow speeds than at apastron (compare the values of v_{C96} in Table 7). This explains why the model gives relatively narrow lines for CXO$_{001119}$, even though there is material flowing almost directly toward and away from the observer, and why the model gives lines blueshifted by a few hundred km s^{-1} for CXO$_{030616}$, even though the angle between the flow velocity and the line of sight is large (see Fig. 22).

We repeated the above fitting with the S XVI Lyα line. In general, it could not discriminate between different sets of orbital parameters as strongly as the Si XIV line, but of those that we investigated, $i = 70°$, $\omega = 210°$ matched the observed S XVI profiles the best. Table 7 also shows the best-fitting values of f_v and x_{peak} for S XVI. The values of f_v for Si XIV and S XVI are in good agreement. This is as expected, as f_v is a parameter describing the global flow properties of the wind-wind collision, and so it should not be line dependent.

The best-fit values of f_v imply that material is flowing along the wind-wind collision surface at higher speed than is given by the Cantó et al. (1996) equations. Far from the stagnation point, v_{C96} approaches ~900 km s^{-1}. However, the best-fit values of f_v imply that the speed along the collision surface approaches ~2000 km s^{-1}, which is a significant fraction of the terminal velocity of the companion (~3000 km s^{-1}; Pittard & Corcoran 2002). It is expected from hydrodynamical simulations of the wind-wind collision that the flow speed of the shocked gas approaches the terminal velocity of the companion far from the stagnation point.

It should be noted that in the above we do not take into account any line-of-sight velocity due to orbital motion. The observed velocity profile is actually a combination of the projected flow velocity and the orbital velocity of the line-emitting region. Orbital motion would make the profiles more redshifted if the companion is moving away from the observer before periastron, and vice versa. However, the flow velocity dominates, and we find that we cannot get a reliable estimate of the orbital motion of the line-emitting region from the data. It should also be noted that even if we could measure the orbital motion of the line-emitting region, it would not be a direct measure of the orbital motion of the companion. If we could localize the line-emitting region in space, then we could in principle relate its motion to that of companion, but in practice this would be difficult to do.

5.3. The Effect of Bound-Free Absorption on the Observed Line Shapes

Henley et al. (2003) showed that bound-free absorption could have a profound effect on the shapes of the X-ray emission lines observed from colliding wind binaries, due to differing absorbing columns through the stars' unshocked winds to different parts of the line-emitting region. When a colliding wind binary is viewed at quadrature, in the absence of any absorption the profiles would be broad, double peaked, and symmetric about the rest wavelength. However, the absorption of the redshifted emission from the far side of the system can result in a profile which is strongly positively skewed, with a blueshifted peak and a tail extending to the red.

We have investigated the effect of absorption on our profiles by calculating optical depths through the wind of the companion star to different points on the wind-wind collision. If we assume the wind is spherically symmetric and non-accelerating, these optical depths can be calculated analytically (Ignace 2001). For portions of the emitting regions which are viewed through the companion's wind, we can parameterize the strength of the absorption due to the companion's wind with the quantity

$$\tau_0 = \frac{\kappa \dot{M}_c}{4\pi v_c D},\qquad(9)$$

where D is the stellar separation and κ is the opacity at the wavelength of the line of interest.

We have repeated the fitting described in the previous section, with the addition of τ_0 as a free parameter. With this modification, we find that we are able to get a good fit (judged by eye) to the Si XIV and S XVI lines for $\omega = 270°$, $i = 50°$ and $\omega = 180°$, $i = 50°$ (i.e., we do not have to assume a new orientation, as we did in the previous section). This is shown in Figure 23, which compares the models with and without absorption for $\omega = 270°$ and $180°$ with the observed MEG -1 Si XIV line from CXO$_{030616}$ (we choose this observation to illustrate our point because the original model gave a particularly poor fit to this observaton for $\omega = 270°$ and $180°$).

The lower part of Table 7 shows the best-fitting model parameters for the Si XIV and S XVI lines with absorption included in the model. This set of results is for the orbital orientation $\omega = 270°$, $i = 50°$. Note again that the values of f_v for the two lines are in good agreement with each other, as expected. Note also that the values of x_{peak} for the two lines are less variable than in the model without absorption, and also that they are in good agreement with each other. The orbit of η Car with $e = 0.95$ and $\omega = 270°$ is shown in Figure 22 (cf. Fig. 17). Figure 22 also shows the approximate location of the Si XIV emitting region for CXO$_{001119}$ and CXO$_{030616}$.

The results of this modeling are discussed in §6.2.

6. DISCUSSION

The X-ray emission lines of η Car show clear variability, becoming blueshifted and broader just before the X-ray minimum in mid-2003. This variability cannot be described by a simple geometrical model of the wind-wind collision in which the emission originates from a conical surface with constant opening angle with a longitude of periastron of $\omega \approx 270°$, which is the value consistent with modeling of the X-ray 2–10 keV flux variations (Corcoran et al. 2001a) and from analysis of the absorption components in He I P-Cygni features (Nielsen et al. 2007). However, we found that a more physical model which describes the shape of the contact surface and the spatial distribution of the X-ray line emissivity along the contact surface, and which takes into account absorption in the unshocked wind of the companion, was able to match the observed HETGS line profiles at all phases with $\omega = 270°$ and $i = 50°$.

Because of the simplifying assumptions inherent in the line profile model, and the uncertainty of the input parameters, it is possible that other values of ω and i could be made to fit the observed X-ray line profiles. It should also be emphasized that we did not attempt to find a global best-fitting solution, and so $\omega = 270°$, $i = 50°$ is not necessarily the best-fitting set of orbital parameters. Indeed, we found we could also get a good fit to the X-ray line profiles with $\omega = 180°$. However, the important result is that we have shown that a colliding wind model can explain the observed line profile variations, without having to invoke any additional flow component (Behar et al. 2007).

6.1. Comparison to Line Profiles of Other Massive Stars

Massive stars are believed to produce X-rays via any or all of the following processes: by wind-wind collisions in binary stars or multiple systems ("colliding wind" emission); by intrinsic shocks embedded in the unstable, radiatively driven winds ("intrinsic wind" emission); and via the magnetic field confinement of the radiatively driven wind ("magnetically confined" emission).

Stars in which intrinsic wind X-ray emission dominates the observed emission generally show strong line emission but little emission at wavelengths shortward of 3 Å. X-ray emission from a few of these systems have been observed at high spectral resolution. The emission lines are generally broad, with HWHM ≈ 1000 km s^{-1}, which is typically half the terminal wind velocity. Leutenegger et al. (2006) presented a uniform analysis of the helium-like lines in four O stars (ζ Ori, ζ Pup, ι Ori and δ Ori) and showed that these stars had rather stronger intercombination lines and lower $\mathcal{R}$ values than we find in the η Car spectra; typically the $\mathcal{R}$

ratio was near 2–3 for the Si XIII triplet, while the $\mathcal{R}$ ratio was 1.0 ± 0.4 for S XV in ζ Pup (the only star for which S XV could be measured). While ι Ori and ζ Ori are binaries, and δ Ori is a multiple system, none of these four stars show any strong evidence of X-ray emission from wind-wind collisions, and X-rays from all these stars are believed to be dominated by the emission from intrinsic shocks embedded within the winds of the stars themselves. The $\mathcal{R}$ ratios from these O stars are about a factor of 2 lower than the $\mathcal{R}$ ratios we measured for η Car (see Table 4), which implies that the minimum radius r_0 of the line-forming region for these stars is fairly near the stars, $1.25 < r_0/r_* < 1.67$ (Leutenegger et al. 2006), where r_* is the stellar radius. The exception to this is the S XV $\mathcal{R}$ ratio from CXO_{021016}, which is similar to the value measured from ζ Pup. An intriguing possibility is that we are seeing intrinsic emission from the companion's wind. If this is the case, it raises the question of why we see this effect in only one observation.

Colliding wind systems generally show thermal X-ray emission, sometimes at wavelengths shortward of 3 Å, and may show strong iron K-shell emission. Pollock et al. (2005) found that in the long-period, eccentric colliding wind binary WR 140 that the intercombination lines in all the measured He-like lines in that star were very weak, and noted differences between the weak intercombination lines in WR 140 and the stronger i components observed in O star spectra. The intercombination lines are similarly weak in the shorter-period eccentric colliding wind system γ^2 Velorum (Skinner et al. 2001; Henley et al. 2005).

Like the colliding wind systems, magnetically confined winds can show thermal X-ray emission shortward of 3 Å. The best-studied examples of this class are θ^1 Ori C and τ Sco. Both stars show hard X-ray emission which is modulated by the rotation of the star, giving rise to variations on much shorter timescales than either the "intrinsic wind" emitters or the colliding wind systems. X-ray emission line profiles from shocked gas in "magnetically confined" winds are typically fairly narrow and usually show symmetric profiles. An analysis of θ^1 Ori C by Gagné et al. (2005) showed that the observed emission lines were relatively narrow ($\sim$ few hundred km s^{-1}) and that the line centroids are close to zero velocity independent of viewing angle. This contrasts with the observed variable line profiles we see in η Car.

6.2. Constraining the Interaction Region

The X-ray line profiles offer the most sensitive diagnostic of the flow of the shocked gas produced by the wind-wind interaction in η Car, and one of the few spectral diagnostics which can be unambiguously localized. We have shown that simple geometrical models in which the interaction region is a conical surface do not do a good job in describing the changes

in both line widths and line centroids for any assumed orbital orientation (the longitude of periastron ω), orbital inclination or eccentricity. A more physical model based on the Cantó et al. (1996) analytical "thin-shell" geometry of the wind-wind collision interface provides a reasonable description of the line profile shapes at all of the observed phases for values of eccentricity which are consistent with analyses of the broad-band X-ray fluxes and the He I P Cygni absorptions. If we do not include absorption in the model, the value of ω we derive from the line profile modeling (210°) is significantly less than the value of $\omega = 275°$ used in the modeling of the *RXTE* X-ray lightcurve by Corcoran et al. (2001a), although it is close to the value of $\omega = 200°$ derived by Ishibashi (2001) from his analysis of the *RXTE* data. However, when we take into account the effect of bound-free absorption in the unshocked wind of the companion, we find we can get a good fit to the profiles with $\omega = 270°$. We use the model parameters obtained for this latter model (from Table 7) in the following discussion. Our profile analysis is consistent with models in which periastron occurs near superior conjunction, i.e., when the companion star is behind η Car as viewed by the observer on earth. This is in contrast to the analysis of η Car's millimeter wavelength flux variations (Abraham et al. 2005a,b) and the He II 4686 Å line radial velocity curve (Abraham & Falceta-Gonçalves 2007), which both concluded that periastron occurs near inferior conjunction.

We first discuss the best-fitting values of τ_0 in Table 7. We can equation (9) to derive the mass-loss rate of the companion from τ_0. For the opacity we use cross-sections from (Bałucińska-Church & McCammon 1992), with a revised He cross-section from Yan et al. (1998), and solar abundances (Anders & Grevesse 1989). Using the stellar separations in Table 7, and assuming $v_c = 3000$ km s^{-1} for the wind speed of the companion (Pittard & Corcoran 2002), the best-fitting values of τ_0 in Table 7 imply mass-loss rates for the companion of 0.6×10^{-5} $M_\odot$ yr^{-1} for CXO$_{001119}$ to 5.2×10^{-5} $M_\odot$ yr^{-1} for CXO$_{030616}$ (cf. 10^{-5} $M_\odot$ yr^{-1} derived by Pittard & Corcoran 2002 from their modeling of the CXO$_{001119}$ spectrum, using hydrodynamical models of the wind-wind collsion). Rather than indicating a true variation in the mass-loss rate of the companion, the apparent variation may be a result of the emission region being smaller at periastron than at apastron. As a result, the lines of sight to the emission region are more likely to pass through the wind acceleration zone close to the companion, where the densities are higher. These higher densities would enhance the absorption, giving a higher τ_0 in the fitting, and hence a higher mass-loss rate.

As the absorption cross-section at the energy of the S XVI line is approximately half that at the energy of the Si XIV line (Bałucińska-Church & McCammon 1992), one would expect the best-fitting values of τ_0 for S XVI to be approximately half the corresponding values for Si XIV. Given the uncertainties, our best-fitting values of τ_0 are consistent with this expectation.

The best-fitting values of x_{peak} for Si XIV and S XVI are similar to each other, implying they originate from similar regions of the wind-wind collision. As Si XIV and S XVI form over a wide range of temperatures with significant overlap, this result is not surprising. Indeed, models of X-ray line emission in colliding wind binaries based on hydrodynamical simulations show that S XVI and Si XIV are expected to form in similar regions of the wind-wind collision (see Fig. 2 in Henley et al. 2003).

We have compared our measured values of x_{peak} with those expected from hydrodynamical simulations of the wind-wind collision. We use similar hydrodynamical models to those discussed in Pittard & Corcoran (2002), which include radiative cooling, and use the line-profile model of Henley et al. (2003) to determine the distance from the stagnation point at which the X-ray emission is expected to peak, assuming collisional ionization equilibrium. The values of x_{peak} expected from these models are plotted in Figure 24. Away from periastron ($\phi = 1$), the model values of x_{peak} are fairly constant. This is as expected if radiative cooling is unimportant, because for adiabatic colliding wind shocks the structure of the wind-wind collision scales self-similarly with binary separation (Stevens et al. 1992). As a result, we would expect x_{peak} (in units of the stellar separation) to be constant with orbital phase for a given line. As the system approaches periastron, the increasing post-shock densities make radiative cooling more important, and as a result the size the emitting region shrinks. Figure 24 shows that the model values of x_{peak} rapidly decrease as the system approaches periastron.

Figure 24 also shows the observed values of x_{peak} for Si XIV and S XVI from the lower part of Table 7. The observed values of x_{peak} do not match the values expected from hydrodynamical simulations. Away from periastron the observed values are $\sim$7–10 times smaller than the model values. Also, the observed value of x_{peak} does not rapidly fall just before periastron. Instead, x_{peak} is fairly constant at $\sim$0.1. Therefore, away from periastron the observed lines are forming closer to the stagnation point than is expected from the hydrodynamical simulations. This may be because cooling in the shocked gas is more rapid than pure radiative cooling, perhaps due to inverse Compton cooling or mixing with cool material. This increased cooling would result in a smaller emission region than would be expected if only radiative cooling were operating. However, this enhanced cooling is unlikely to be more important at apastron, when the densities are lower, than at periastron – just before periastron ($\phi = 0.992$; CXO_{030616}), the observed and model values of x_{peak} are in better agreement. An alternative explanation is that the shocked gas is out of equilibrium. The lower post-shock densities away from apastron may mean that the ionization temperature lags behind the kinetic temperature after the gas has been shock heated. As a result, the Si XIV and S XVI emission would tend to originate closer to the stagnation point than would be expected if the gas were in equilibrium – if the gas were in equilibrium, it would be too

hot near the stagnation point for Si XIV and S XVI. As the system approaches periastron, the post-shock densities increase, and the shocked gas starts to equilibrate. By itself, this equilibration would tend to increase the size of the emission region, as the gas near the stagnation point becomes too hot for Si XIV and S XVI. However, as the system approaches periastron, radiative cooling becomes more important, which tends to reduce the size of the emission region. Our observed values of x_{peak} suggest that, as the system approaches periastron, the increase in the size of the emission region due to the gas equilibrating is canceled by the decrease in the size of the emission region due to radiative cooling, resulting in a roughly constant observed value of x_{peak}. More detailed hydrodynamical modeling, including modeling of the post-shock ionization evolution, is required to see if the above-described scenario is likely. Such modeling is beyond the scope of this paper. However, we can in principle estimate whether or not non-equilibrium ionization is likely to be important by comparing the ionization timescale to the flow timescale, using equation (14) from Henley et al. (2005). We find the ratio of the ionization timescale to the flow timescale is 0.94 for CXO_001119, 0.56 for CXO_021016, and 0.23 for CXO_030502. Unfortunately, these results are inconclusive: as the ratios are neither much greater than nor much less than unity, it is difficult to state with certainty whether or not non-equilibrium effects are expected in these observations. As radiative cooling is more important for CXO_030616, the appropriate ratio to calculate is that of the ionization timescale to the radiative timescale (eq. [15] from Henley et al. 2005), which is 0.01. As this ratio is much less than unity, this implies that the system is in equilibrium just before periastron, as we have suggested above.

The fact that x_{peak} is roughly constant implies that strong cooling is not affecting the Si XIV and S XVI emission as the system approaches periastron – if it were, the emitting region would decrease in size relative to the stellar separation, as regions further from the stagnation point would become too cool to emit. In contrast to this, Hamaguchi et al. (2007) and Paper II present evidence of cooling in the X-ray–emitting plasma based on excess emission on the low energy side of the Fe XXV triplet near periastron, caused by rapid cooling driving the hot gas out of equilibrium as the stars approach one another. However, it is possible that while the high densities near the stagnation point result in strong cooling in that region, where the Fe XXV emission originates, cooling is less important further out, where the S XVI and Si XIV emission originates. Even if the shocked material is cooling rapidly near the stagnation point, it is still possible to have material hot enough to emit S XVI and Si XIV further out, because material is being shock-heated all along the shock surface.

If the shocked gas is in equilibrium, then the innermost region, nearest the apex of the shock cone, is too hot to emit much silicon or sulfur line emission. We take the inner region of the shock cone where the S XVI emissivity is less than 50% of its maximum emissivity to be the region where the temperature is high enough that sulfur is almost completely ionized,

and assume that the Fe XXV and Fe XXVI emission originates from somewhere in this region. This assumption constrains the iron K-shell region to be on the surface of the wind-wind interface within about 0.14 AU just before periastron. If, as discussed above, the shocked gas is not in equilibrium in the earlier observations, we cannot use this method to constrain the size the iron K-shell region near apastron.

7. CONCLUSIONS

We have presented our analysis of resolved silicon and sulfur X-ray emission lines from a series of HETGS observations of η Car at key orbital phases. These lines originate in the wind-wind collision zone where the slow, dense wind of η Car interacts with the fast, low-density wind of a massive companion star. We have shown that line profile variations around the orbit are not consistent with simple geometrical models of the line forming region. A more physically realistic model which takes into account the detailed geometry of the contact discontinuity and allows for variations in the emissivity distribution along the shock boundary can produce both the variations in the line centroids and the observed changes in line width. This analysis allows us to probe directly both the temperature distribution along the shock boundary and also the flow of the shocked wind of the companion away from the stagnation point at the apex of the shock.

The Si XIV and S XVI emission appear to originate from similar regions, which is as expected given the range of temperatures at which they are produced. However, away from periastron they originate closer to the stagnation point than is expected from hydrodynamical simulations. This may be because the wind-wind collision is out of equilibrium. Just before periastron the size of the Si XIV-emitting region is closer to that which is expected from hydrodynamical simulation, suggesting that the shocked gas has equilibrated at the time of CXO_{030616}. We find that the flow speed along the wind-wind collision surface is $\sim 3\times$ the flow speed given by the analytic model of Cantó et al. (1996). This larger flow speed approaches a large fraction of the terminal velocity of the companion star's wind far from the stagnation point, which is in fair agreement with detailed numerical hydrodynamic models of the flow.

We can obtain a good fit to the profiles with an inclination and longitude of periastron similar to those which have previously been assumed ($i \approx 50°$ and $\omega \approx 270°$), although this is only true if we include the effects of absorption by the unshocked wind of the companion. Given the simplifying assumptions inherent in the model, the uncertainty of the various input model parameters, and the fact that we did not search for a global best fit, we cannot rule out other possible orbital orientations. Nevertheless, an important result of this analysis is that it shows that colliding wind models can fit the detailed flow dynamics as shown by

the variations in X-ray line profiles, without recourse to additional flows in the system.

These results must be considered preliminary since the observed line profile variations need to be confirmed as dependent on orbital phase rather than simply secular changes in the wind. A *Chandra* HETGS observation is scheduled for 2007 October, and ideally more will be carried out around the time of the next X-ray minimum, expected in 2009 January. These observations will complement ongoing X-ray monitoring with *RXTE* and ground-based optical and radio observations. Meanwhile, the line profile model can be improved by the inclusion of more realistic absorption from the wind of η Car and from the wind of the companion star, which might give further insight into the mass loss rate of the wind from the companion, and by more detailed numerical models including turbulence to directly determine the dependence of the theoretical line profiles on the orientation and geometry of the colliding wind region.

REFERENCES

Abraham, Z., & Falceta-Gonçalves, D. 2007, MNRAS, 378, 309

Abraham, Z., Falceta-Gonçalves, D., Dominici, T., Caproni, A., & Jatenco-Pereira, V. 2005a, MNRAS, 364, 922

Abraham, Z., Falceta-Gonçalves, D., Dominici, T. P., Nyman, L.-Å., Durouchoux, P., McAuliffe, F., Caproni, A., & Jatenco-Pereira, V. 2005b, A&A, 437, 977

Anders, E., & Grevesse, N. 1989, Geochim. Cosmochim. Acta, 53, 197

Bałucińska-Church, M., & McCammon, D. 1992, ApJ, 400, 699

Behar, E., Nordon, R., & Soker, N. 2007, ApJ, 666, L97

Behar, E., Rasmussen, A. P., Griffiths, R. G., Dennerl, K., Audard, M., Aschenbach, B., & Brinkman, A. C. 2001, A&A, 365, L242

Blumenthal, G. R., Drake, G. W. F., & Tucker, W. H. 1972, ApJ, 172, 205

Cantó, J., Raga, A. C., & Wilkin, F. P. 1996, ApJ, 469, 729

Cash, W. 1979, ApJ, 228, 939

Corcoran, M. F. 2005, AJ, 129, 2018

Corcoran, M. F., Ishibashi, K., Swank, J. H., & Petre, R. 2001a, ApJ, 547, 1034

Corcoran, M. F., Swank, J. H., Petre, R., Ishibashi, K., Davidson, K., Townsley, L., Smith, R., White, S., Viotti, R., & Damineli, A. 2001b, ApJ, 562, 1031

Damineli, A. 1996, ApJ, 460, L49

Damineli, A., Conti, P. S., & Lopes, D. F. 1997, NewA, 2, 107

Damineli, A., Kaufer, A., Wolf, B., Stahl, O., Lopes, D. F., & de Araújo, F. X. 2000, ApJ, 528, L101

Davidson, K., Gull, T. R., Humphreys, R. M., Ishibashi, K., Whitelock, P., Berdnikov, L., McGregor, P. J., Metcalfe, T. S., Polomski, E., & Hamuy, M. 1999, AJ, 118, 1777

Davidson, K., & Humphreys, R. M. 1997, ARA&A, 35, 1

Davidson, K., Ishibashi, K., Gull, T. R., Humphreys, R. M., & Smith, N. 2000, ApJ, 530, L107

Dere, K. P., Landi, E., Mason, H. E., Monsignori Fossi, B. C., & Young, P. R. 1997, A&AS, 125, 149

Duncan, R. A., & White, S. M. 2003, MNRAS, 338, 425

Duncan, R. A., White, S. M., Lim, J., Nelson, G. J., Drake, S. A., & Kundu, M. R. 1995, ApJ, 441, L73

Falceta-Gonçalves, D., Abraham, Z., & Jatenco-Pereira, V. 2006, MNRAS, 371, 1295

Gagné, M., Oksala, M. E., Cohen, D. H., Tonnesen, S. K., ud-Doula, A., Owocki, S. P., Townsend, R. H. D., & MacFarlane, J. J. 2005, ApJ, 628, 986

Gaviola, E. 1950, ApJ, 111, 408

Hamaguchi, K., Corcoran, M. F., Gull, T., Ishibashi, K., Pittard, J. M., Hillier, D. J., Damineli, A., Davidson, K., Nielsen, K. E., & Kober, G. V. 2007, ApJ, 663, 522

Helsdon, S. F., & Ponman, T. J. 2000, MNRAS, 315, 356

Henley, D. B. 2005, PhD thesis, University of Birmingham

Henley, D. B., Stevens, I. R., & Pittard, J. M. 2003, MNRAS, 346, 773

—. 2005, MNRAS, 356, 1308

Hillier, D. J., Davidson, K., Ishibashi, K., & Gull, T. 2001, ApJ, 553, 837

Ignace, R. 2001, ApJ, 549, L199

Iping, R. C., Sonneborn, G., Gull, T. R., Massa, D. L., & Hillier, D. J. 2005, ApJ, 633, L37

Ishibashi, K. 2001, in Astronomical Society of the Pacific Conference Series, Vol. 242, Eta Carinae and Other Mysterious Stars: The Hidden Opportunities of Emission Spectroscopy, ed. T. R. Gull, S. Johannson, & K. Davidson, 53

Ishibashi, K., Corcoran, M. F., Davidson, K., Swank, J. H., Petre, R., Drake, S. A., Damineli, A., & White, S. 1999, ApJ, 524, 983

Leutenegger, M. A., Paerels, F. B. S., Kahn, S. M., & Cohen, D. H. 2006, ApJ, 650, 1096

Lührs, S. 1997, PASP, 109, 504

Markert, T. H., Canizares, C. R., Dewey, D., McGuirk, M., Pak, C. S., & Schattenburg, M. L. 1994, Proc. SPIE, 2280, 168

Martin, J. C., Davidson, K., Humphreys, R. M., Hillier, D. J., & Ishibashi, K. 2006, ApJ, 640, 474

Mewe, R., & Schrijver, J. 1978, A&A, 65, 115

Nielsen, K. E., Corcoran, M. F., Gull, T. R., Hillier, D. J., Hamaguchi, K., Ivarsson, S., & Lindler, D. J. 2007, ApJ, 660, 669

Pittard, J. M., & Corcoran, M. F. 2002, A&A, 383, 636

Pittard, J. M., Stevens, I. R., Corcoran, M. F., & Ishibashi, K. 1998, MNRAS, 299, L5

Pollock, A. M. T., Corcoran, M. F., Stevens, I. R., & Williams, P. M. 2005, ApJ, 629, 482

Press, W. H., Teukolsky, S. A., Vetterling, W. T., & Flannery, B. P. 1992, Numerical Recipes in C, 2nd edn. (Cambridge: Cambridge University Press)

Seward, F. D., Forman, W. R., Giacconi, R., Griffiths, R. E., Harnden, F. R., Jones, C., & Pye, J. P. 1979, ApJ, 234, L55

Skinner, S. L., Güdel, M., Schmutz, W., & Stevens, I. R. 2001, ApJ, 558, L113

Smith, N. 2004, MNRAS, 351, L15

Smith, N., Morse, J. A., Collins, N. R., & Gull, T. R. 2004, ApJ, 610, L105

Smith, R. K., Brickhouse, N. S., Liedahl, D. A., & Raymond, J. C. 2001, ApJ, 556, L91

Steiner, J. E., & Damineli, A. 2004, ApJ, 612, L133

Sterken, C., de Groot, M. J. H., & van Genderen, A. M. 1996, A&AS, 116, 9

Stevens, I. R., Blondin, J. M., & Pollock, A. M. T. 1992, ApJ, 386, 265

Verner, E., Bruhweiler, F., & Gull, T. 2005, ApJ, 624, 973

Weisskopf, M. C., Brinkman, B., Canizares, C., Garmire, G., Murray, S., & Van Speybroeck, L. P. 2002, PASP, 114, 1

Whitelock, P. A., Feast, M. W., Koen, C., Roberts, G., & Carter, B. S. 1994, MNRAS, 270, 364

Whitelock, P. A., Feast, M. W., Marang, F., & Breedt, E. 2004, MNRAS, 352, 447

Yan, M., Sadeghpour, H. R., & Dalgarno, A. 1998, ApJ, 496, 1044

Young, P. R., Del Zanna, G., Landi, E., Dere, K. P., Mason, H. E., & Landini, M. 2003, ApJS, 144, 135

Table 1.   *Chandra*-HETGS Observations of η Carinae

Observation ID[a]	Observation ID[b]	Start date	Phase[c] ϕ	Exposure (ks)	HEG Counts[d]	HEG Rate (s^{-1})	MEG Counts[d]	MEG Rate (s^{-1})
CXO$_{001119}$	632	2000 Nov 19	0.528	89.5	18459	0.206	20772	0.232
CXO$_{021016}$	3749	2002 Oct 16	0.872	91.2	38160	0.418	45038	0.493
CXO$_{030502}$	3745	2003 May 2	0.970	94.5	78264	0.828	81925	0.867
CXO$_{030616}$	3748	2003 Jun 16	0.992	97.2	42411	0.436	40553	0.417
CXO$_{030720}$	3746	2003 Jul 20	1.009	90.3	1183	0.013	1725	0.019
CXO$_{030926}$	3747	2003 Sep 26	1.043	70.1	11137	0.159	8098	0.116

[a]Observation identification used in this paper (after Hamaguchi et al. 2007).

[b]Official *Chandra* observation identification.

[c]Mid-observation phase, calculated using the emphemeris in Corcoran (2005).

[d]Total number of first-order (+1 and −1) non-background-subtracted counts.

Table 2. Emission Line Fit Results

Ion (1)	Line (2)	λ_0 (Å) (3)	λ_{obs} (Å) (4)	$\Delta\lambda$ (FWHM) (mÅ) (5)	Flux (10^{-5} ph cm^{-2} s^{-1}) (6)	EW (Å) (7)	Fitting method (8)
			CXO$_{001119}$				
S XVI	Lyα	4.7274	4.7267 ± 0.0012	20.2 ± 4.9	2.96 ± 0.34	0.041 ± 0.005	(a)
S XV	r	5.0387	5.0366 ± 0.0007	13.7 ± 1.8	4.99 ± 0.41	0.087 ± 0.007	(a)
	i	5.0665	5.0644	13.8	0.97 ± 0.27	0.017 ± 0.005	(a)
	f	5.1015	5.0994	13.9	2.41 ± 0.33	0.042 ± 0.006	(a)
Si XIV	Lyα	6.1804	6.1797 ± 0.0006	16.5 ± 1.7	2.43 ± 0.13	0.117 ± 0.006	(b)
Si XIII	r	6.6479	6.6461 ± 0.0005	12.3 ± 1.3	2.57 ± 0.16	0.171 ± 0.011	(b)
	i	6.6882	6.6864	12.4	0.35 ± 0.09	0.024 ± 0.006	(b)
	f	6.7403	6.7385	12.5	1.75 ± 0.13	0.121 ± 0.009	(b)
			CXO$_{021016}$				
S XVI	Lyα	4.7274	4.7262 ± 0.0006	14.1 ± 2.0	6.97 ± 0.44	0.042 ± 0.003	(b)
S XV	r	5.0387	5.0374 ± 0.0006	13.6 ± 1.5	9.27 ± 0.67	0.068 ± 0.005	(b)
	i	5.0665	5.0652	13.7	3.08 ± 0.49	0.022 ± 0.004	(b)
	f	5.1015	5.1002	13.8	3.79 ± 0.53	0.028 ± 0.004	(b)
Si XIV	Lyα	6.1804	6.1772 ± 0.0005	23.3 ± 1.6	5.62 ± 0.23	0.103 ± 0.004	(b)
Si XIII	r	6.6479	6.6458 ± 0.0004	13.8 ± 1.1	4.89 ± 0.23	0.133 ± 0.006	(b)
	i	6.6882	6.6861	13.9	0.50 ± 0.12	0.014 ± 0.003	(b)
	f	6.7403	6.7382	14.0	3.08 ± 0.18	0.087 ± 0.005	(b)
			CXO$_{030502}$				
S XVI	Lyα	4.7274	4.7221 ± 0.0006	21.0 ± 1.9	11.38 ± 0.58	0.043 ± 0.002	(b)
S XV	r	5.0387	5.0335 ± 0.0009	22.1 ± 2.0	11.45 ± 0.78	0.066 ± 0.005	(b)
	i	5.0665	5.0613	22.2	3.34 ± 0.59	0.017 ± 0.004	(b)
	f	5.1015	5.0962	22.4	5.71 ± 0.68	0.027 ± 0.004	(b)
Si XIV	Lyα	6.1804	6.1698 ± 0.0005	33.7 ± 1.4	7.68 ± 0.26	0.125 ± 0.004	(b)
Si XIII	r	6.6479	6.6397 ± 0.0006	24.6 ± 1.6	5.55 ± 0.27	0.122 ± 0.005	(b)
	i	6.6882	6.6800	24.7	0.62 ± 0.16	0.014 ± 0.004	(b)
	f	6.7403	6.7322	24.9	3.52 ± 0.22	0.080 ± 0.005	(b)
			CXO$_{030616}$				
S XVI	Lyα	4.7274	4.7213 ± 0.0009	22.6 ± 2.8	4.96 ± 0.39	0.051 ± 0.004	(b)
S XV	r	5.0387	5.0312 ± 0.0008	21.5 ± 2.2	8.18 ± 0.56	0.113 ± 0.008	(b)
	i	5.0665	5.0590	21.6	2.50 ± 0.41	0.036 ± 0.006	(b)
	f	5.1015	5.0939	21.8	4.63 ± 0.45	0.068 ± 0.007	(b)
Si XIV	Lyα	6.1804	6.1667 ± 0.0007	28.3 ± 1.9	2.92 ± 0.15	0.130 ± 0.007	(b)
Si XIII	r	6.6479	6.6329 ± 0.0009	35.7 ± 2.2	3.42 ± 0.20	0.244 ± 0.014	(b)
	i	6.6882	6.6731	35.9	0.34 ± 0.13	0.025 ± 0.010	(b)
	f	6.7403	6.7251	36.2	2.30 ± 0.16	0.172 ± 0.012	(b)
			CXO$_{030720}$				
S XVI	Lyα	4.7274	4.7299 ± 0.0041	21.8 ± 9.7	0.19 ± 0.06	0.085 ± 0.027	(a)
S XV	r	5.0387	5.0374 ± 0.0015	13.8 ± 4.0	0.63 ± 0.13	0.177 ± 0.037	(a)
	i	5.0665	5.0652	13.9	0.14 ± 0.08	0.038 ± 0.022	(a)
	f	5.1015	5.1002	14.0	0.45 ± 0.11	0.113 ± 0.029	(a)
Si XIV	Lyα	6.1804	6.1766 ± 0.0019	12.1 ± 5.3	0.16 ± 0.03	0.098 ± 0.020	(a)
Si XIII	r	6.6479	6.6421 ± 0.0013	19.8 ± 3.6	0.58 ± 0.07	0.372 ± 0.048	(c)
	i	6.6882	6.6824	19.9	0.05 ± 0.03	0.035 ± 0.022	(c)

Table 2—Continued

Ion	Line	λ_0 (Å)	λ_{obs} (Å)	$\Delta\lambda$ (FWHM) (mÅ)	Flux (10^{-5} ph cm^{-2} s^{-1})	EW (Å)	Fitting method
(1)	(2)	(3)	(4)	(5)	(6)	(7)	(8)
	f	6.7403	6.7344	20.1	0.36 ± 0.06	0.248 ± 0.039	(c)
			CXO$_{030926}$				
S XVI	Lyα	4.7274	4.7291 ± 0.0020	8.0 ± 7.0	0.50 ± 0.11	0.048 ± 0.011	(a)
S XV	r	5.0387	5.0370 ± 0.0012	11.9 ± 3.4	1.09 ± 0.19	0.167 ± 0.030	(a)
	i	5.0665	5.0648	12.0	0.48 ± 0.15	0.076 ± 0.023	(a)
	f	5.1015	5.0998	12.0	0.48 ± 0.14	0.077 ± 0.023	(a)
Si XIV	Lyα	6.1804	6.1763 ± 0.0032	25 ± 10	0.24 ± 0.06	0.103 ± 0.025	(a)
Si XIII	r	6.6479	6.6452 ± 0.0021	20.2 ± 4.6	0.25 ± 0.06	0.147 ± 0.035	(a)
	i	6.6882	6.6855	20.3	0.03 ± 0.03	0.016 ± 0.019	(a)
	f	6.7403	6.7376	20.5	0.21 ± 0.05	0.128 ± 0.032	(a)

Note. — Values without quoted errors were tied to other fit parameters. Col. (3): Rest wavelengths from ATOMDB v1.3.1. For each Lyα line we give the wavelengths of the brighter component; the wavelengths of the fainter components are 4.7328 Å (S XVI) and 6.1858 Å (Si XIV). Col. (4): Observed wavelength. Col. (5): Observed line width. Col. (6): Observed line flux. For each Lyα line we give the flux of the brighter component; the fluxes of the fainter components are half of these values. Col. (7): Equivalent width. Col. (8): (a) Fitting to HEG ± 1 and MEG ± 1 simultaneously; (b) Fitting to HEG ± 1 and MEG ± 1 individually and averaging the results. (c) Fitting to MEG ± 1 simultaneously.

Table 3. Emission Line Shifts And Widths

Ion	Shift (km s^{-1})	Width (FWHM) (km s^{-1})
CXO$_{001119}$		
S XVI	-44 ± 76	1281 ± 311
S XV	-125 ± 42	815 ± 107
Si XIV	-34 ± 29	800 ± 82
Si XIII	-81 ± 23	555 ± 59
CXO$_{021016}$		
S XVI	-76 ± 38	894 ± 127
S XV	-77 ± 36	809 ± 89
Si XIV	-155 ± 24	1131 ± 78
Si XIII	-95 ± 18	623 ± 50
CXO$_{030502}$		
S XVI	-336 ± 38	1333 ± 121
S XV	-309 ± 54	1316 ± 119
Si XIV	-514 ± 24	1637 ± 68
Si XIII	-370 ± 27	1111 ± 72
CXO$_{030616}$		
S XVI	-387 ± 57	1435 ± 178
S XV	-446 ± 48	1281 ± 131
Si XIV	-665 ± 34	1376 ± 92
Si XIII	-676 ± 41	1614 ± 99
CXO$_{030720}$		
S XVI	$+159 \pm 260$	1382 ± 615
S XV	-77 ± 89	821 ± 238
Si XIV	-184 ± 92	587 ± 257
Si XIII	-262 ± 59	894 ± 162
CXO$_{030926}$		
S XVI	$+108 \pm 127$	507 ± 444
S XV	-101 ± 71	708 ± 202
Si XIV	-199 ± 155	1213 ± 485
Si XIII	-122 ± 95	911 ± 208

Table 4. $\mathcal{R}$ Ratios for Helium-like Ions

Ion	λ_1[a] (Å)	λ_2[a] (Å)	Measured $\mathcal{R}$ Ratios						$\mathcal{R}_0$[b]
			CXO$_{001119}$	CXO$_{021016}$	CXO$_{030502}$	CXO$_{030616}$	CXO$_{030720}$	CXO$_{030926}$	
S XV	738.32	673.40	2.5 ± 0.8	1.2 ± 0.3	1.7 ± 0.4	1.9 ± 0.4	3.1 ± 2.0	1.0 ± 0.4	2.0
Si XIII	865.14	814.69	5.0 ± 1.3	6.2 ± 1.5	5.7 ± 1.5	6.8 ± 2.6	6.9 ± 4.5	7.6 ± 8.9	2.5

Note. — $\mathcal{R} = f/i$, where f and i are the forbidden and intercombination line fluxes, respectively.

[a]Wavelengths to go from the upper level of the forbidden line to the upper levels of the intercombination lines – $\lambda_{1,2}$ are the transition wavelengths for $2\,^3S_1 \rightarrow 2\,^3P_{1,2}$, respectively (from CHIANTI; Dere et al. 1997; Young et al. 2003).

[b]Theoretical low-density, low-UV-flux limit at temperature of maximum emissivity (see eq. [2]; values from Blumenthal et al. 1972).

Table 5. G Ratios for Helium-like Ions

Ion	CXO$_{001119}$	CXO$_{021016}$	CXO$_{030502}$	CXO$_{030616}$	CXO$_{030720}$	CXO$_{030926}$
S XV	0.68 ± 0.10	0.74 ± 0.09	0.79 ± 0.10	0.87 ± 0.10	0.94 ± 0.29	0.89 ± 0.25
Si XIII	0.82 ± 0.08	0.73 ± 0.06	0.75 ± 0.06	0.77 ± 0.08	0.71 ± 0.15	0.97 ± 0.34

Note. — $G = (f + i)/r$, where f, i, and r are the forbidden, intercombination, and resonance line fluxes, respectively.

Table 6. η Carinae Orbital Parameters

Parameter	Value	Reference
T_0 (periastron) (JD)	2 450 799.792	(1)
Period P (d)	2024	(1)
Eccentricity e	0.90	(2)
Longitude of periastron ω (deg)	275	(2)
Inclination i (deg)	50	(2)

Note. — (1) Corcoran (2005); (2) Corcoran et al. (2001a).

Table 7.   Best-fitting Model Parameters from Synthetic Line Profile Modeling

Obs.	D^a (AU)	v_{C96}^b (km s^{-1})	Si XIV x_{peak}^c	τ_0^d	f_v^e	S XVI x_{peak}^c	τ_0^e	f_v^d
			No absorption – results for $\omega = 210°$, $i = 70°$					
CXO$_{001119}$	29.2	200	$0.079^{+0.008}_{-0.007}$ (2.3 AU)	$\cdots$	$2.29^{+0.04}_{-0.02}$	$0.119^{+0.026}_{-0.055}$ (3.5 AU)	$\cdots$	$2.25^{+0.05}_{-0.14}$
CXO$_{021016}$	17.4	340	$0.140^{+0.008}_{-0.007}$ (2.4 AU)	$\cdots$		$0.126^{+0.016}_{-0.013}$ (2.2 AU)	$\cdots$	
CXO$_{030502}$	7.00	820	$0.574^{+0.045}_{-0.041}$ (4.0 AU)	$\cdots$		$0.302^{+0.043}_{-0.029}$ (2.1 AU)	$\cdots$	
CXO$_{030616}$	2.73	850	$0.683^{+0.057}_{-0.053}$ (1.9 AU)	$\cdots$		$0.361^{+0.068}_{-0.041}$ (1.0 AU)	$\cdots$	
			Absorption included in model – results for $\omega = 270°$, $i = 50°$					
CXO$_{001119}$	29.2	200	$0.082^{+0.009}_{-0.008}$ (2.4 AU)	$0.011^{+0.016}_{-0.011}$	$3.08^{+0.08}_{-0.17}$	$0.127^{+0.023}_{-0.020}$ (3.7 AU)	< 0.021	$2.83^{+0.17}_{-0.12}$
CXO$_{021016}$	17.4	340	$0.124^{+0.007}_{-0.006}$ (2.2 AU)	$0.043^{+0.011}_{-0.012}$		$0.115^{+0.013}_{-0.011}$ (2.0 AU)	$0.007^{+0.016}_{-0.007}$	
CXO$_{030502}$	7.00	820	$0.143^{+0.007}_{-0.006}$ (1.0 AU)	$0.192^{+0.014}_{-0.011}$		$0.127^{+0.012}_{-0.010}$ (0.9 AU)	$0.165^{+0.024}_{-0.040}$	
CXO$_{030616}$	2.73	850	$0.107^{+0.006}_{-0.003}$ (0.3 AU)	$0.966^{+0.017}_{-0.038}$		$0.113^{+0.013}_{-0.011}$ (0.3 AU)	$0.30^{+0.16}_{-0.07}$	

[a]Stellar separation in AU, using stellar masses from Corcoran et al. (2001a), orbital period from Corcoran (2005), and eccentricity $e = 0.9$ from §5.2.

[b]Velocity along the contact discontinuity at $x = x_{peak}$ for Si XIV, according to Cantó et al. (1996).

[c]Distance from the stagnation point at which the line luminosity peaks, in units of the stellar separation and (in parentheses) in AU.

[d]Absorption parameter; see equation (9).

[e]Scaling factor by which the velocities calculated from the Cantó et al. (1996) equations are multiplied before calculating model profiles. For each line, the same scaling factor is used for all four observations.
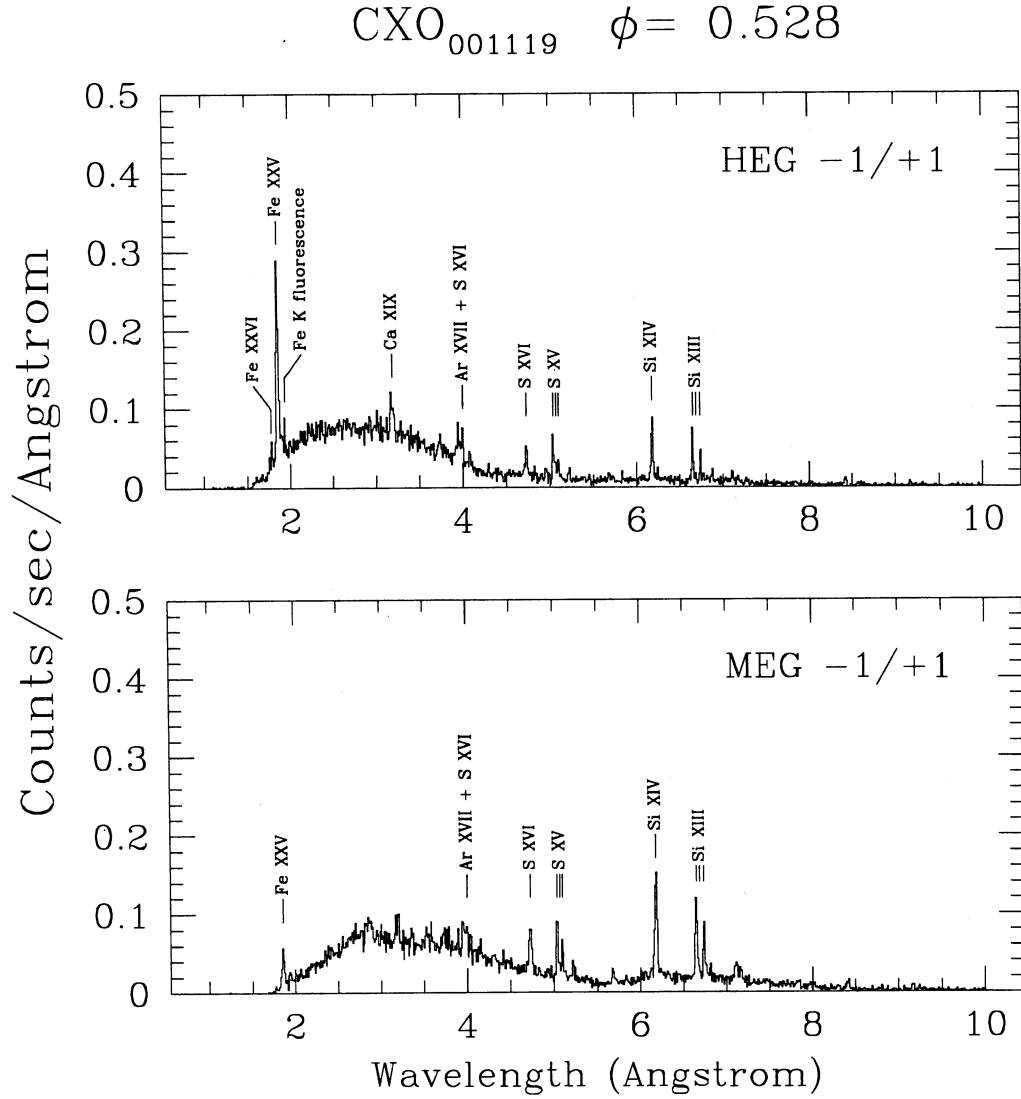
Fig. 1.— *Chandra* HETGS spectra of η Car from CXO$_{001119}$. For each grating (HEG and MEG) the +1 and −1 orders have been co-added, and the spectra have been binned up to 0.01 Å.
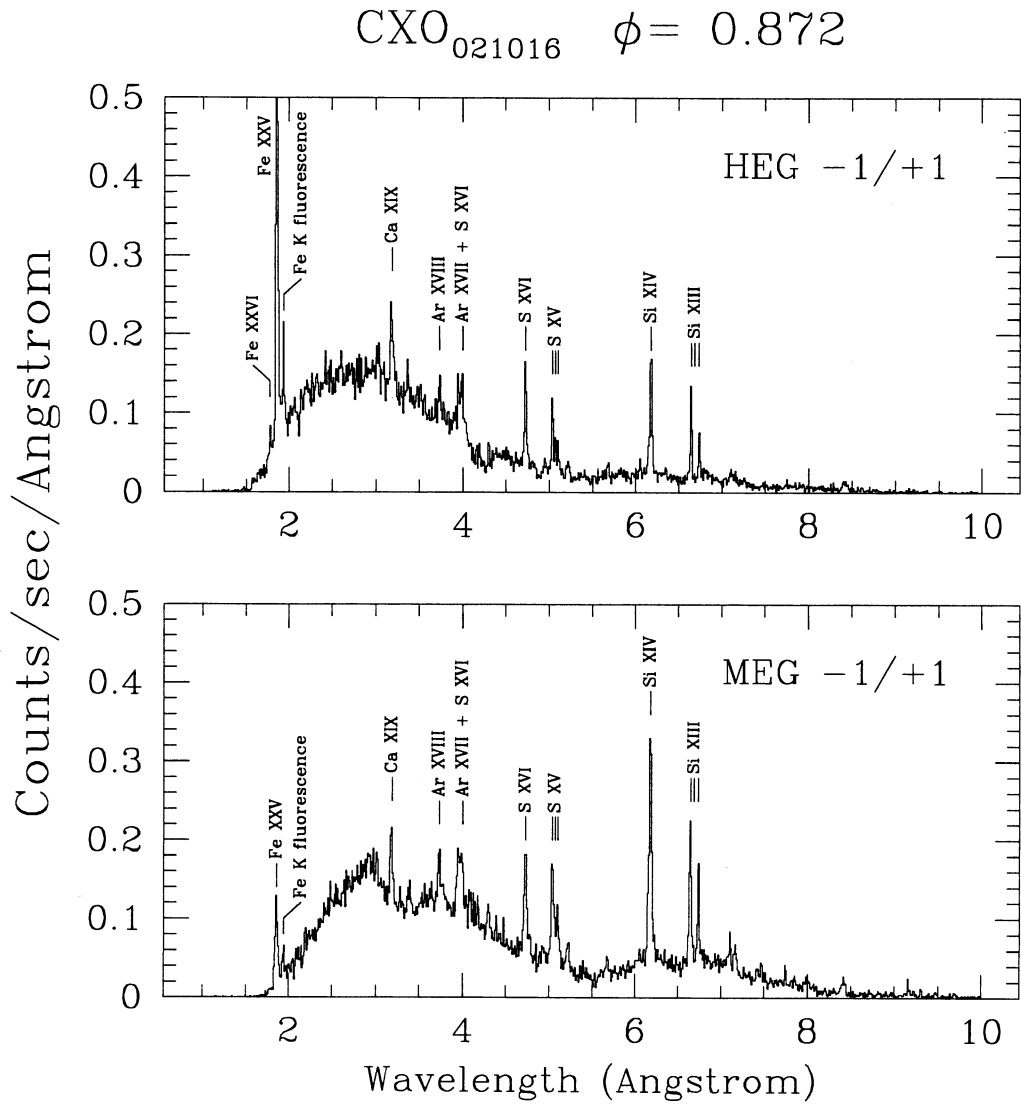
Fig. 2.— As Figure 1, but for CXO$_{021016}$.
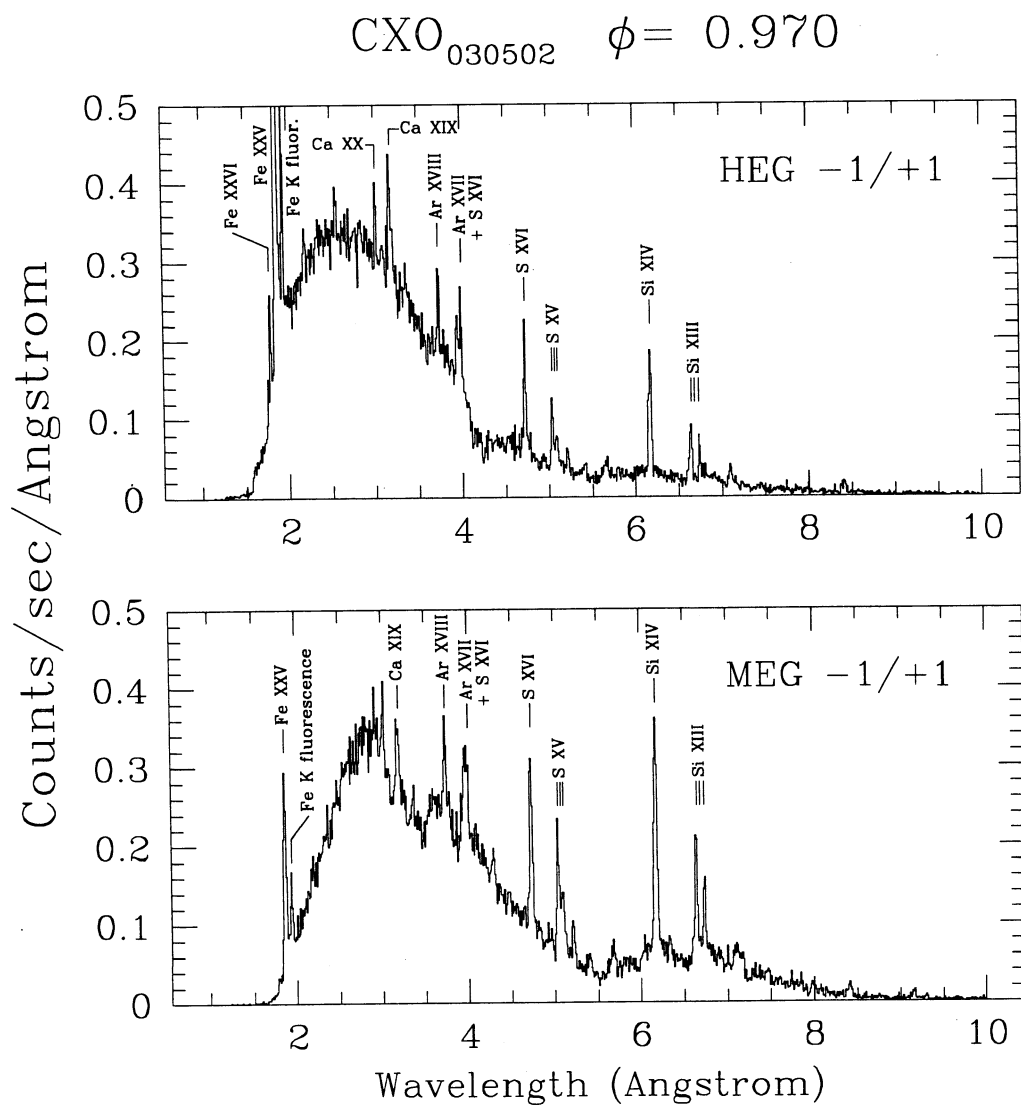
Fig. 3.— As Figure 1, but for CXO$_{030502}$.
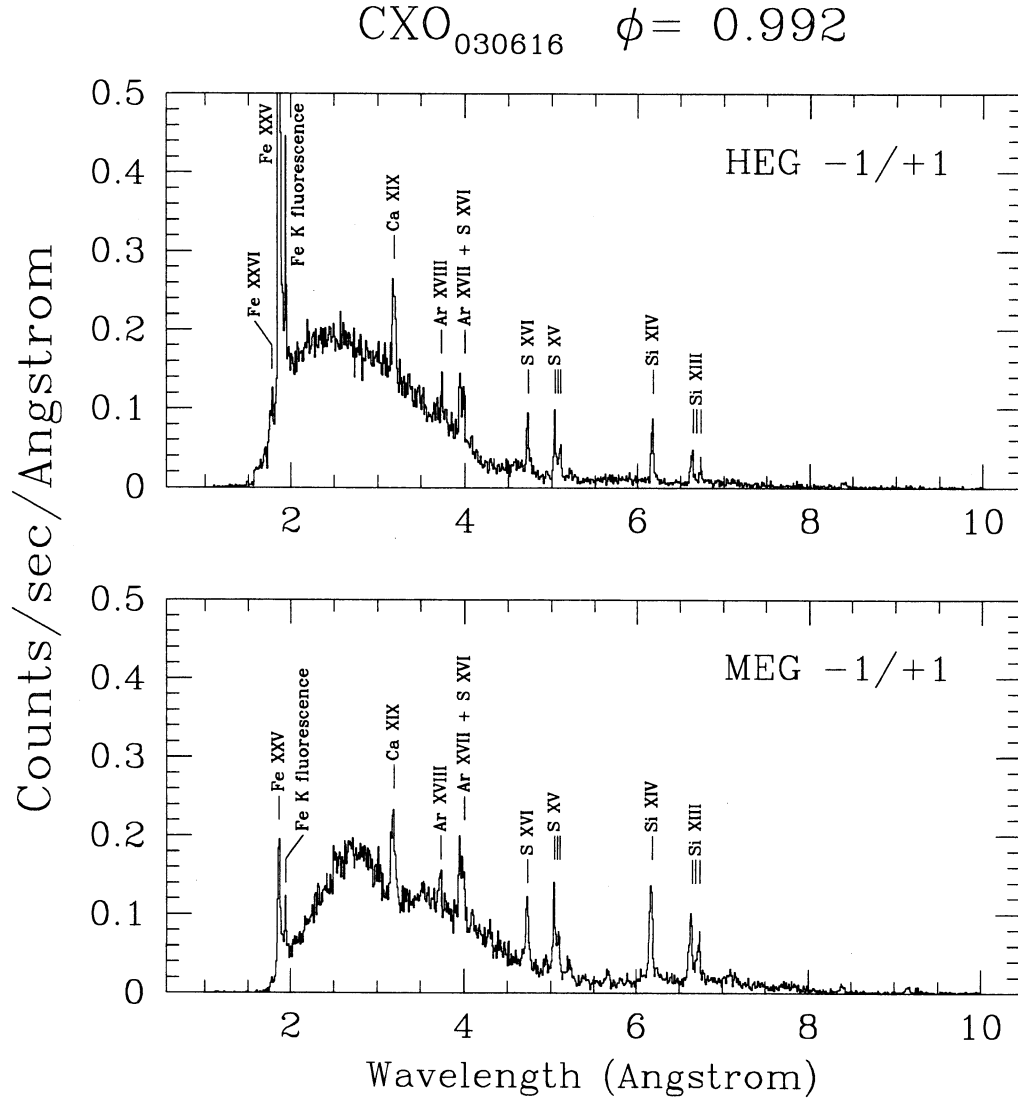
Fig. 4.— As Figure 1, but for CXO_{030616}.
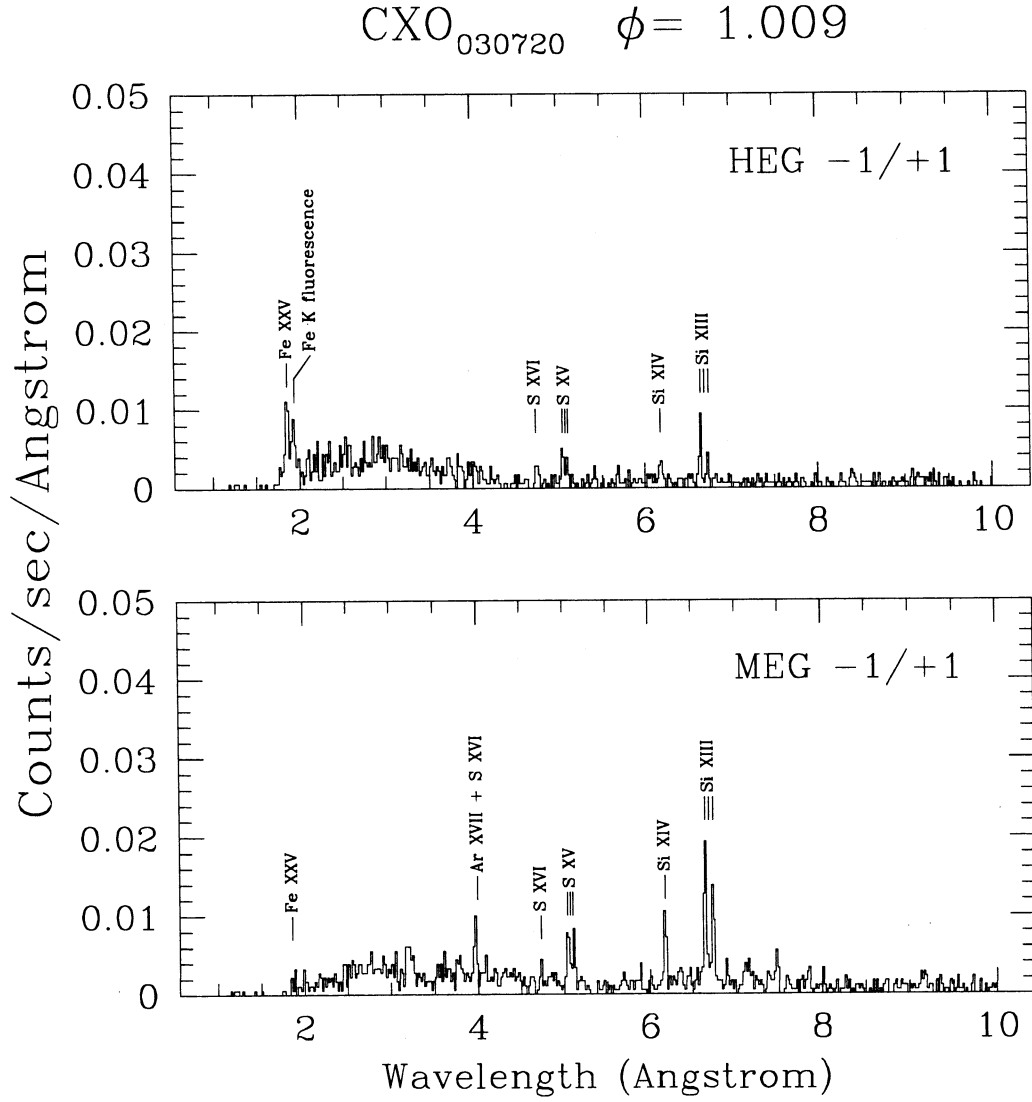
Fig. 5.— As Figure 1, but for CXO_{030720}, with the spectrum binned up to 0.02 Å, instead of 0.01 Å. Note that the y-axis range is different from Figures 1 through 4 and 6.
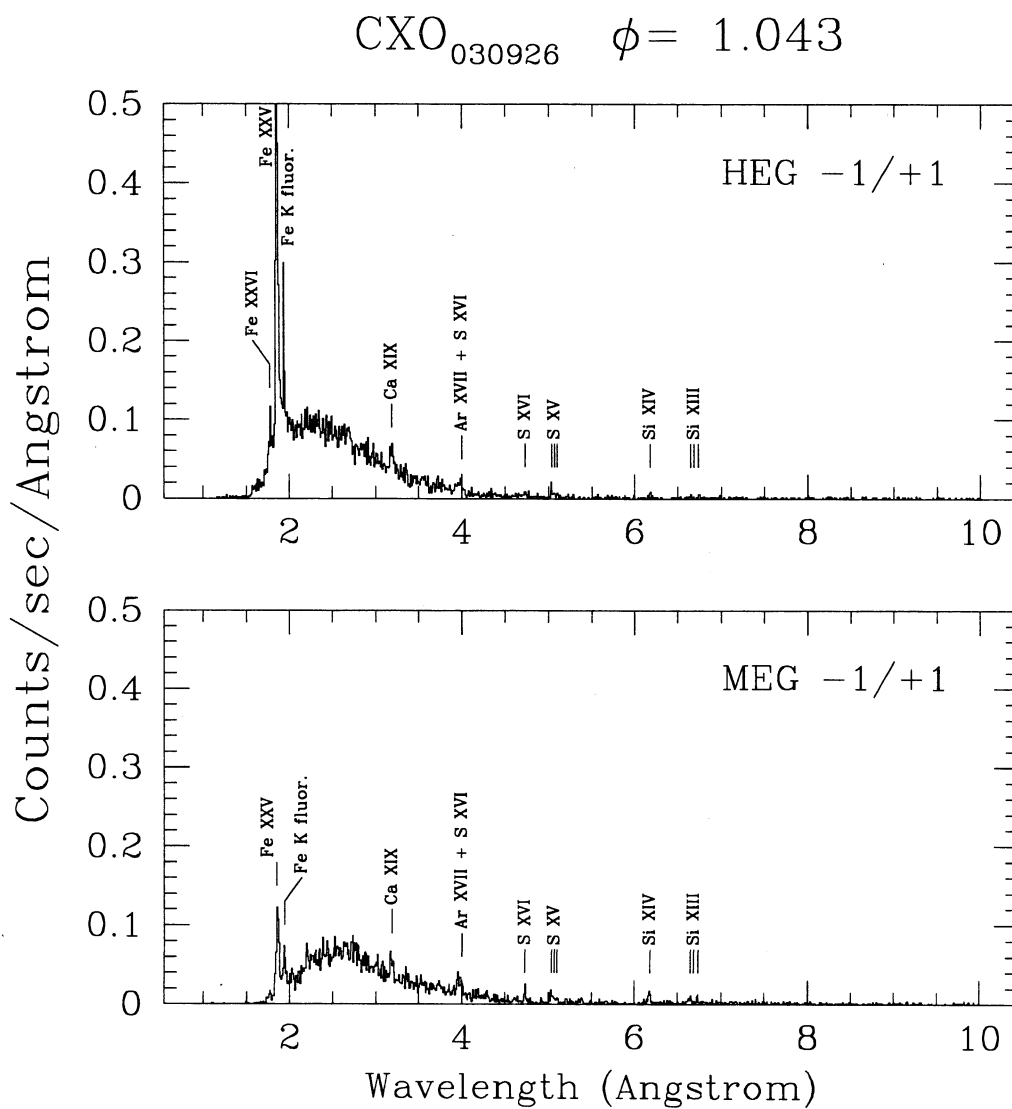
$$\text{CXO}_{030926} \quad \phi = 1.043$$

Fig. 6.— As Figure 1, but for CXO_{030926}.
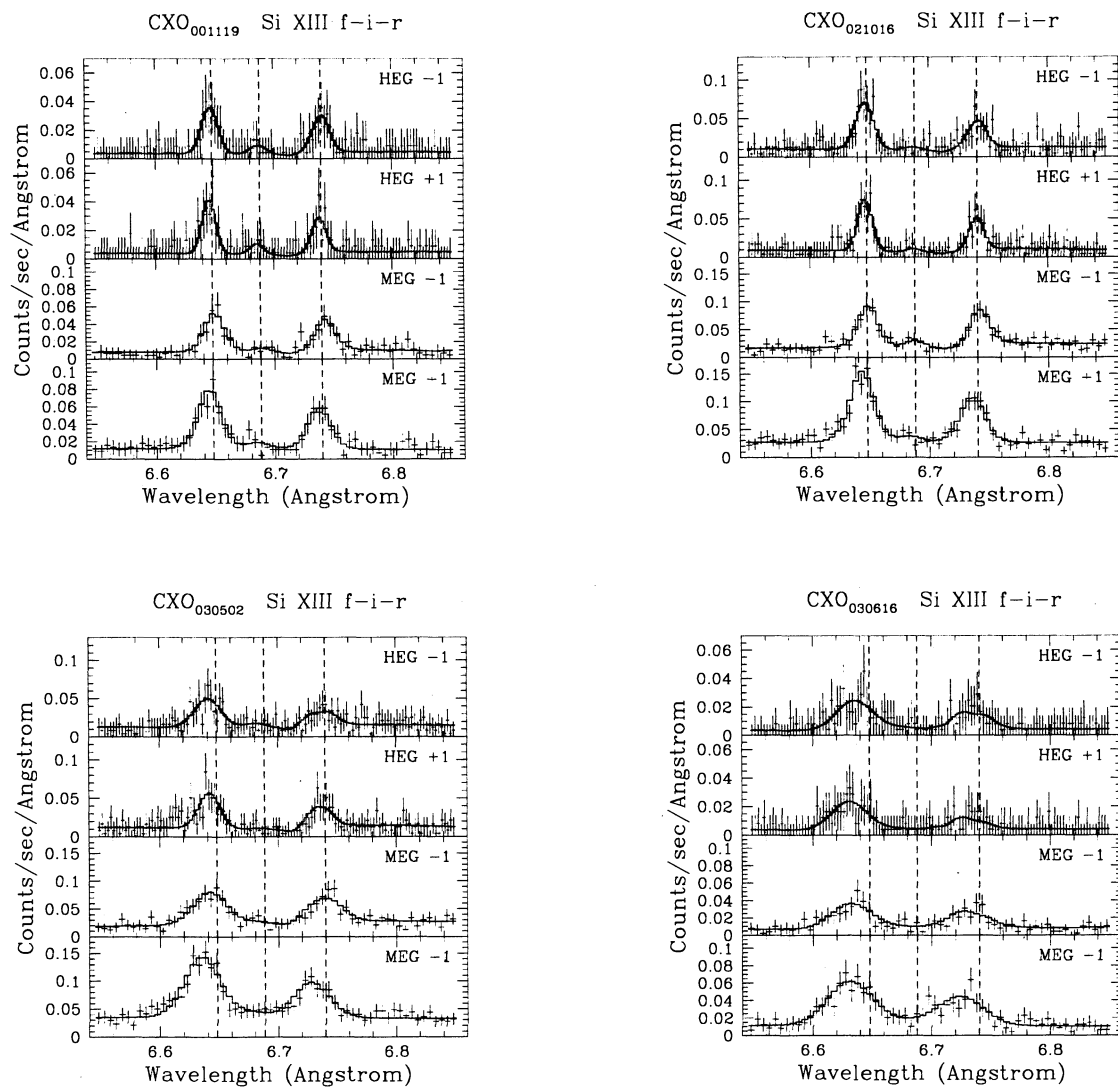
Fig. 7.— Si XIII f-i-r triplets from CXO$_{001119}$, CXO$_{021016}$, CXO$_{030502}$, and CXO$_{030616}$, showing the best-fitting Gaussian line model obtained by fitting to each spectral order individually. The vertical dashed lines show the rest wavelengths of the resonance, intercombination, and forbidden lines (6.6479, 6.6882, and 6.7403 Å, respectively).
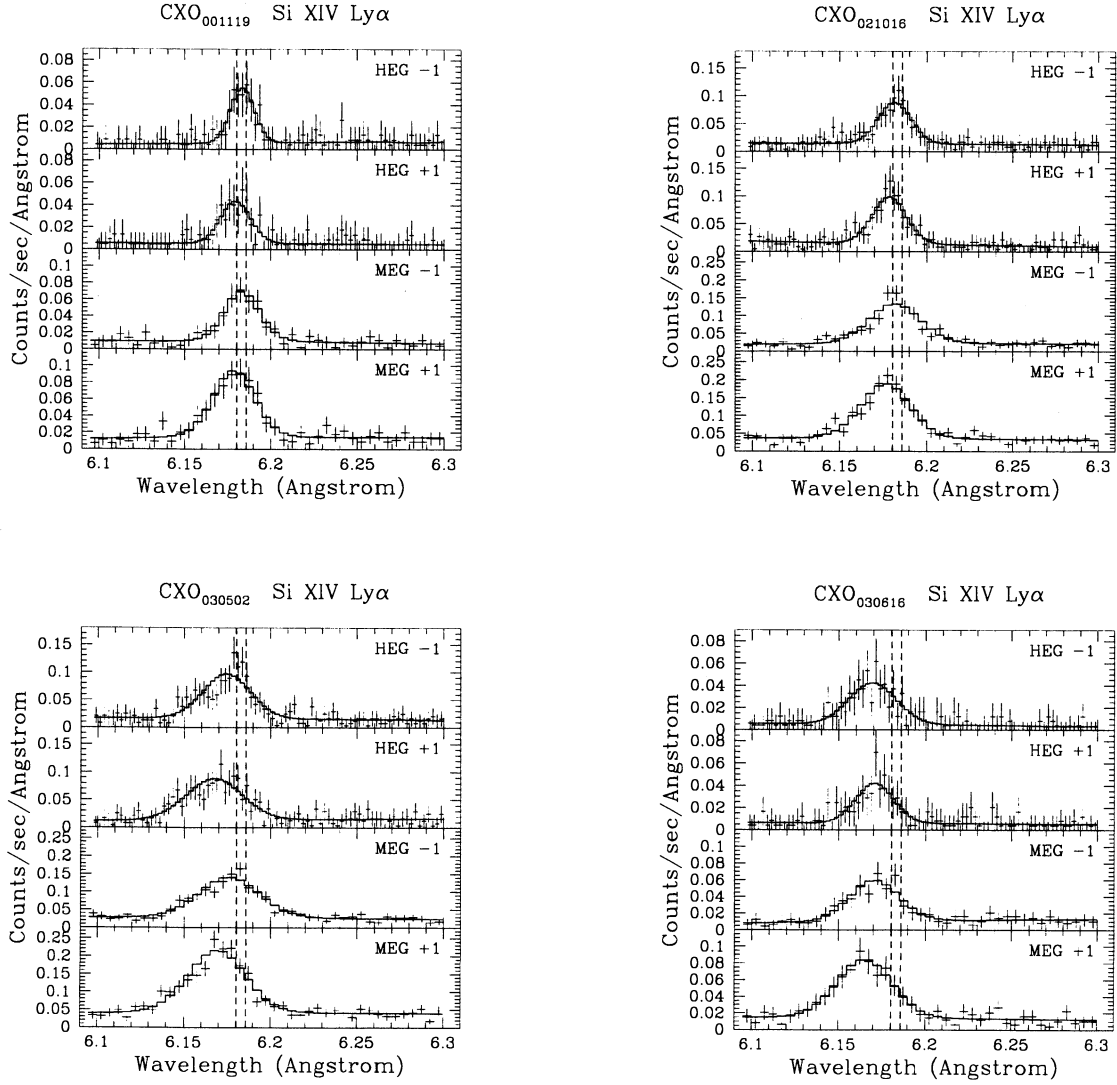
Fig. 8.— As Figure 7, but showing the Si XIV Lyα line. The vertical dashed lines show the rest wavelengths of the two components of the line (6.1804 and 6.1858 Å, respectively).
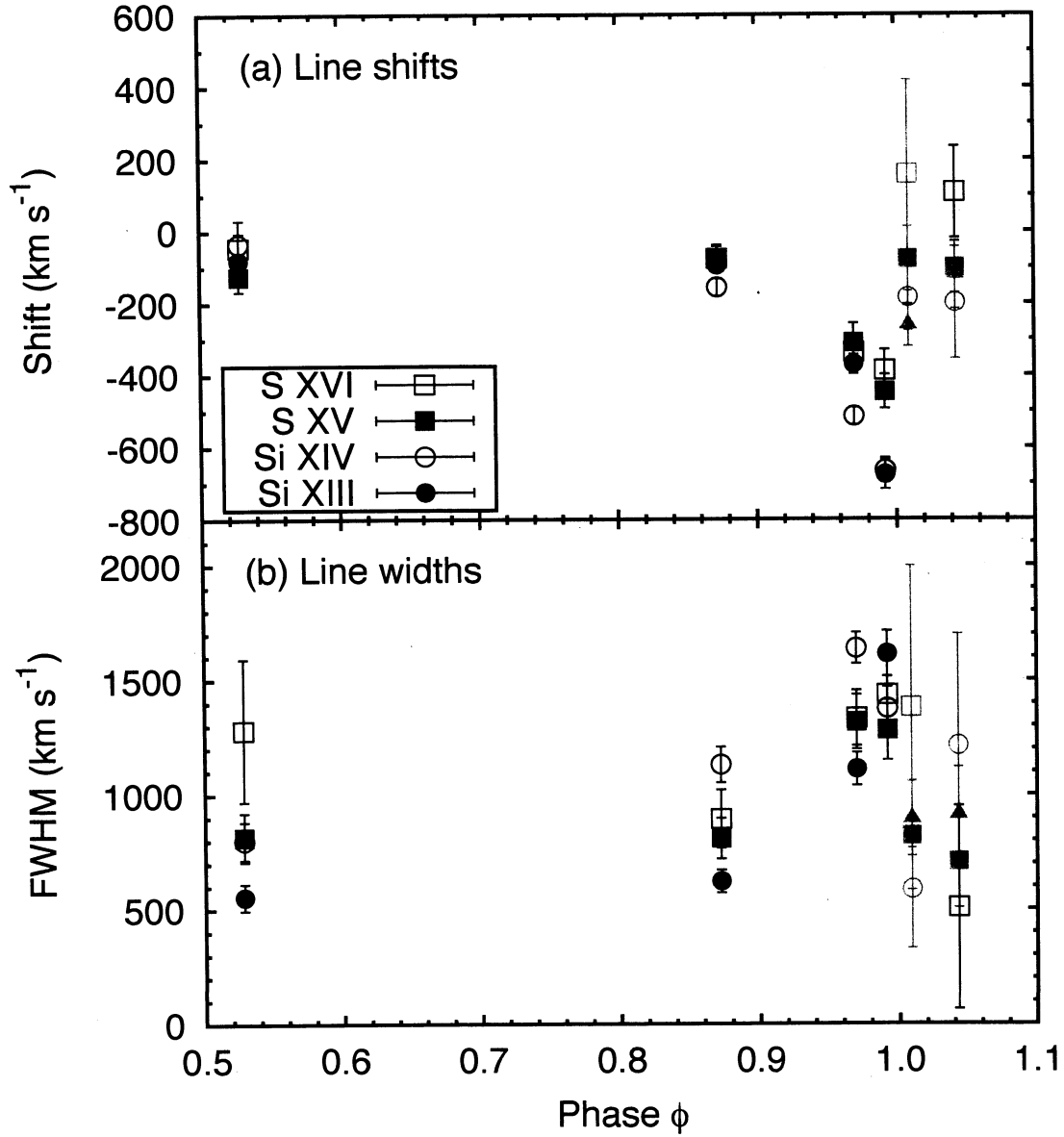
Fig. 9.— Observed emission line shifts (a) and widths (b) plotted against phase. The phase for each observation is taken from Table 1. Phase $\phi = 1$ corresponds to the start of the X-ray minimum in 2003 June. The gray datapoints are for lines contaminated by the CCE component (Hamaguchi et al. 2007).
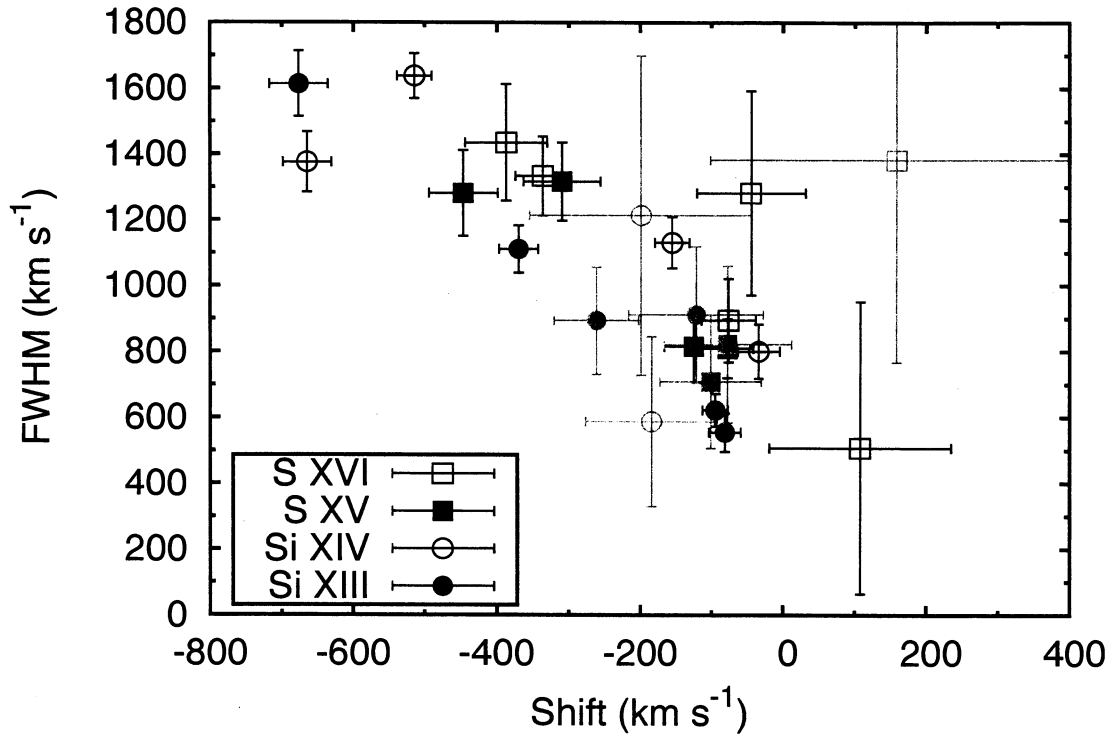
Fig. 10.— The observed emission line widths plotted against the line shifts, showing the correlation between the two. The gray datapoints are for lines contaminated by the CCE component (Hamaguchi et al. 2007).
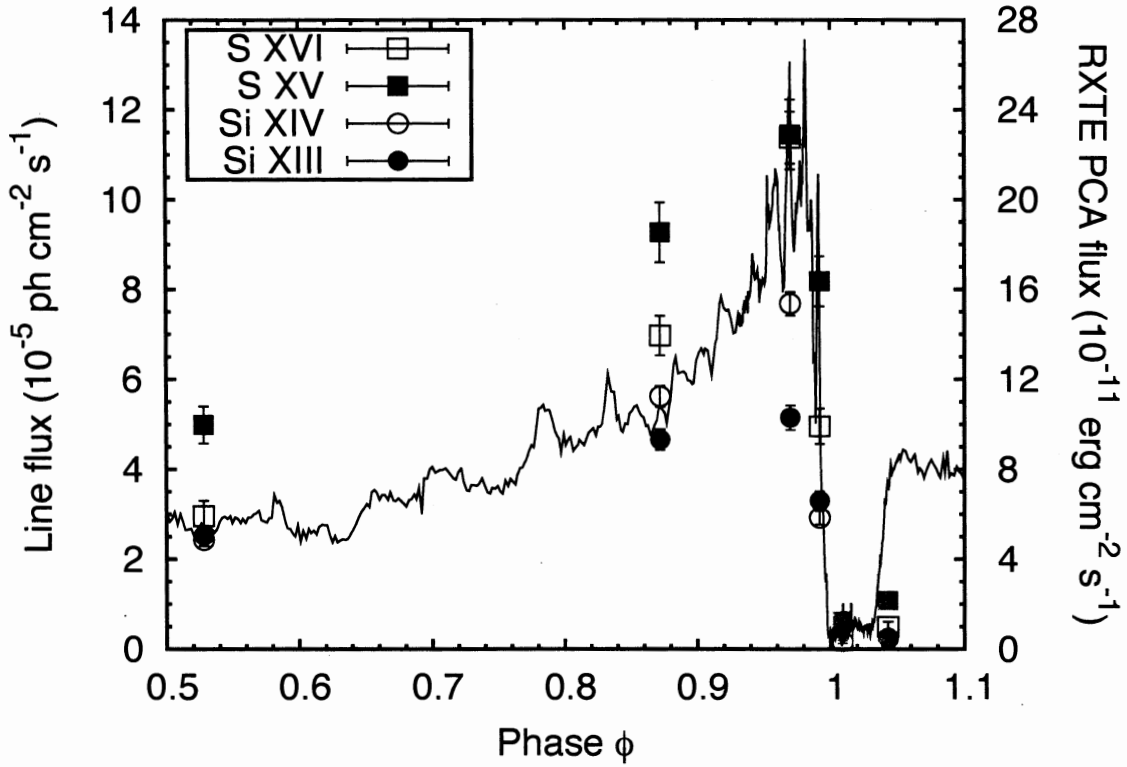
Fig. 11.— Observed emission line fluxes plotted against phase. The phase for each observation is taken from Table 1. Phase $\phi = 1$ corresponds to the start of the X-ray minimum in 2003 June. For S XV and Si XIII we plot the resonance line flux. The solid line shows the 2–10 keV lightcurve measured with *RXTE* (Corcoran 2005). The gray datapoints are for lines contaminated by the CCE component (Hamaguchi et al. 2007).
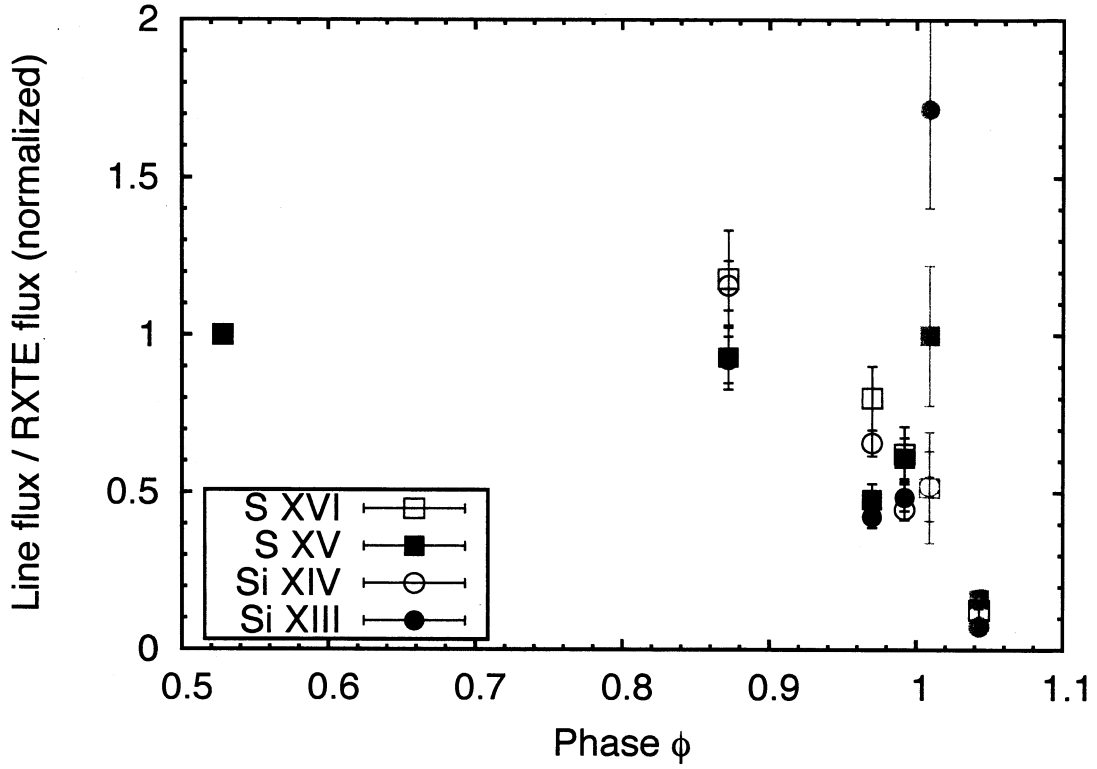
Fig. 12.— Observed emission line fluxes divided by the contemporaneous 2–10 keV flux measured with *RXTE* (Corcoran 2005). For S xv and Si xiii use the resonance line flux. For all lines, the flux ratios have been normalized to the values for phase $\phi = 0.528$ (CXO$_{001119}$). The gray datapoints are for lines contaminated by the CCE component (Hamaguchi et al. 2007).
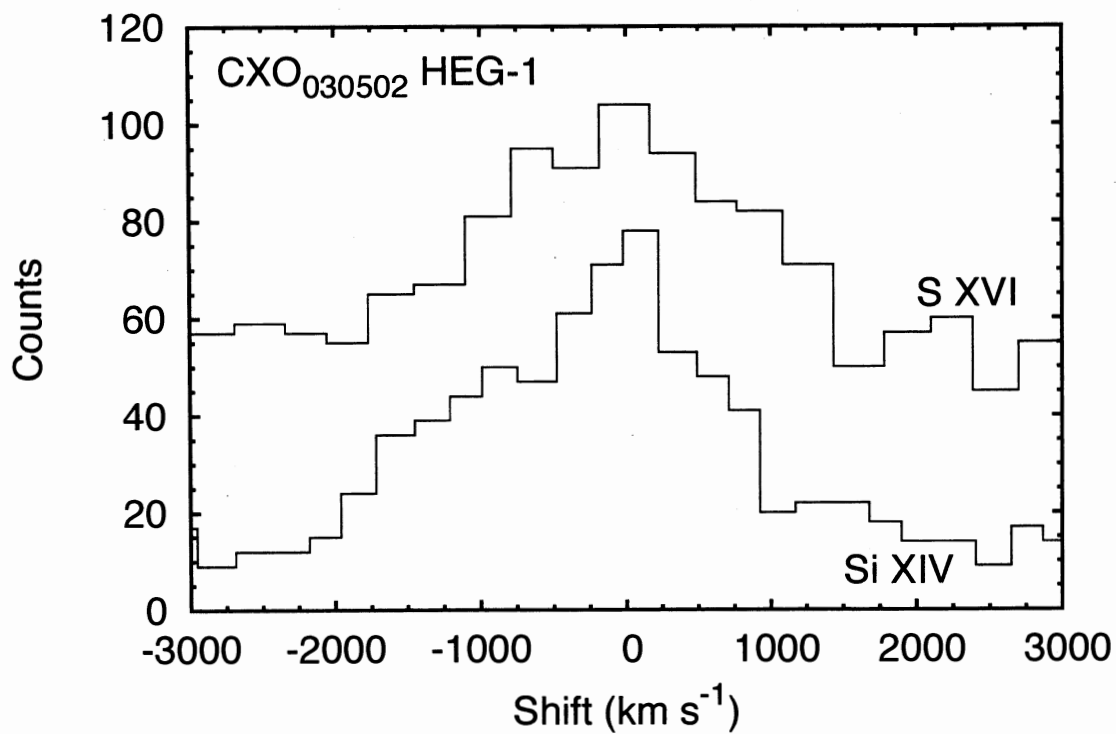
Fig. 13.— Comparison of the HEG −1 profiles of S XVI and Si XIV Lyα from CXO_{030502}. For clarity, the profiles have been binned by a factor of two, and the S XVI profile has been shifted upward by 30 counts.
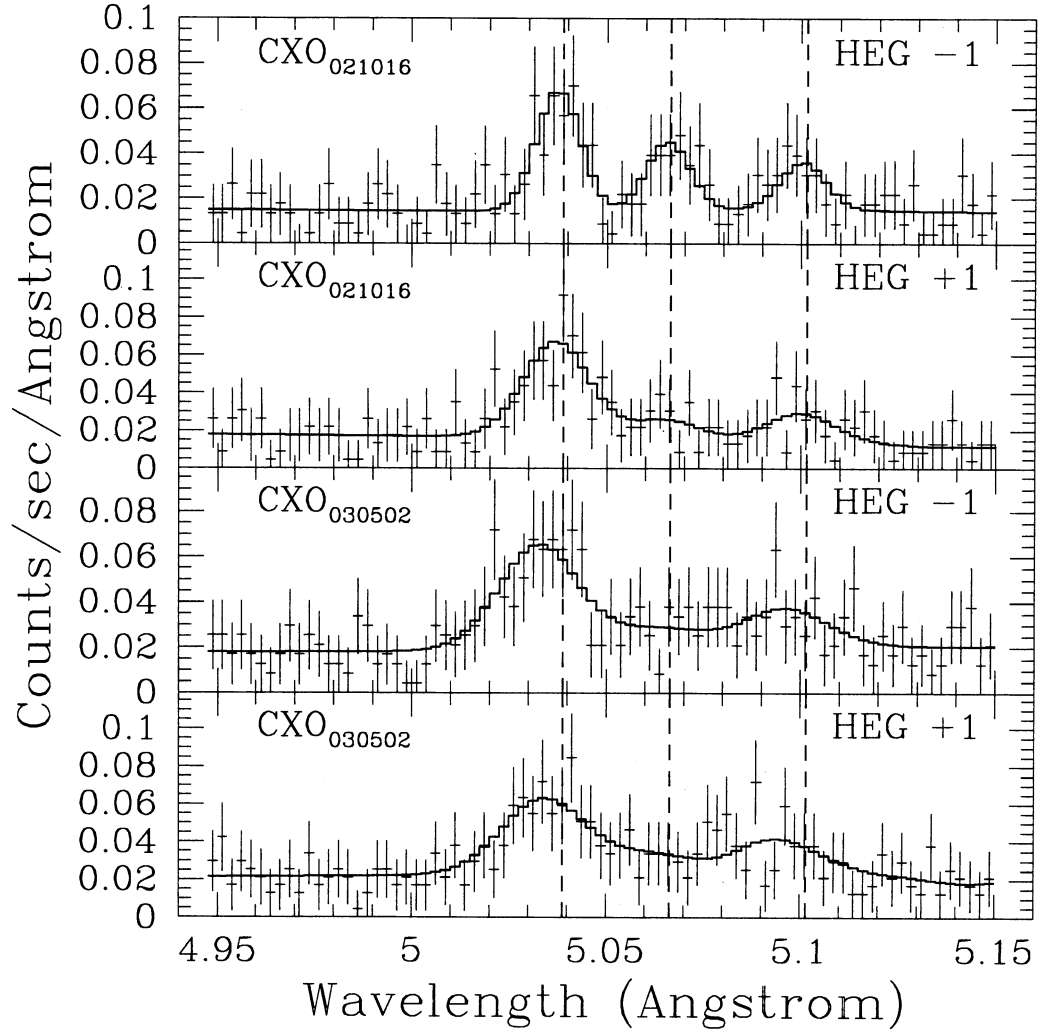
Fig. 14.— First-order HEG spectra of the S xv f-i-r triplet from CXO_{021016} (*top two panels*) and CXO_{030502} (*bottom two panels*). The histograms show the best-fitting Gaussian line models obtained by fitting to each spectral order individually. The vertical dashed lines show the rest wavelengths of the resonance, intercombination, and forbidden lines (5.0387, 5.0665, and 5.1015 Å, respectively).

Si XIII

S XV
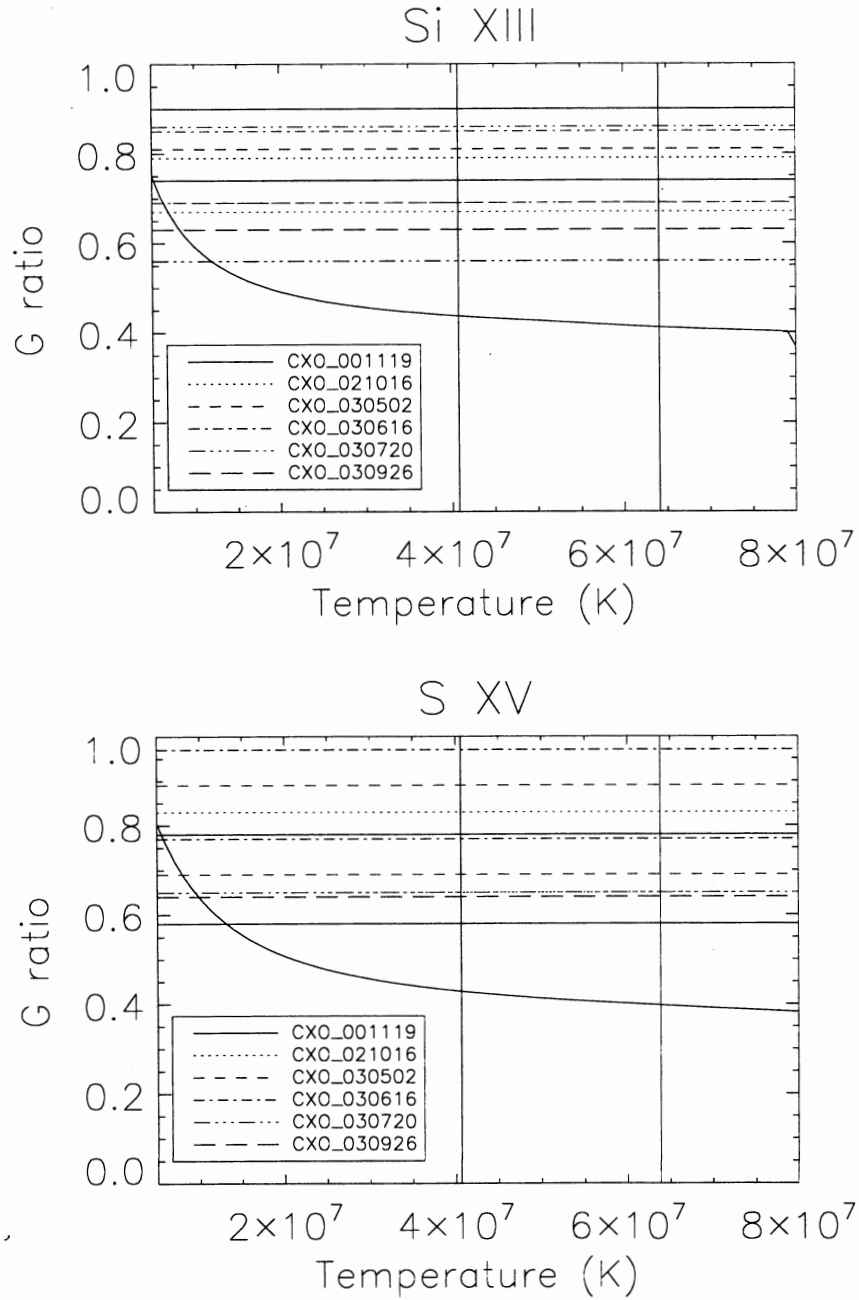
Fig. 15.— $G = (f+i)/r$ ratios for the Si XIII (*top*) and S XV (*bottom*) triplets. The horizontal lines represent the observed values from the different observations. The curved lines show the theoretical values as a function of temperature from APED. The vertical lines are the temperature ranges derived from fitting *XMM-Newton* spectra outside the X-ray minimum (Hamaguchi et al. 2007).
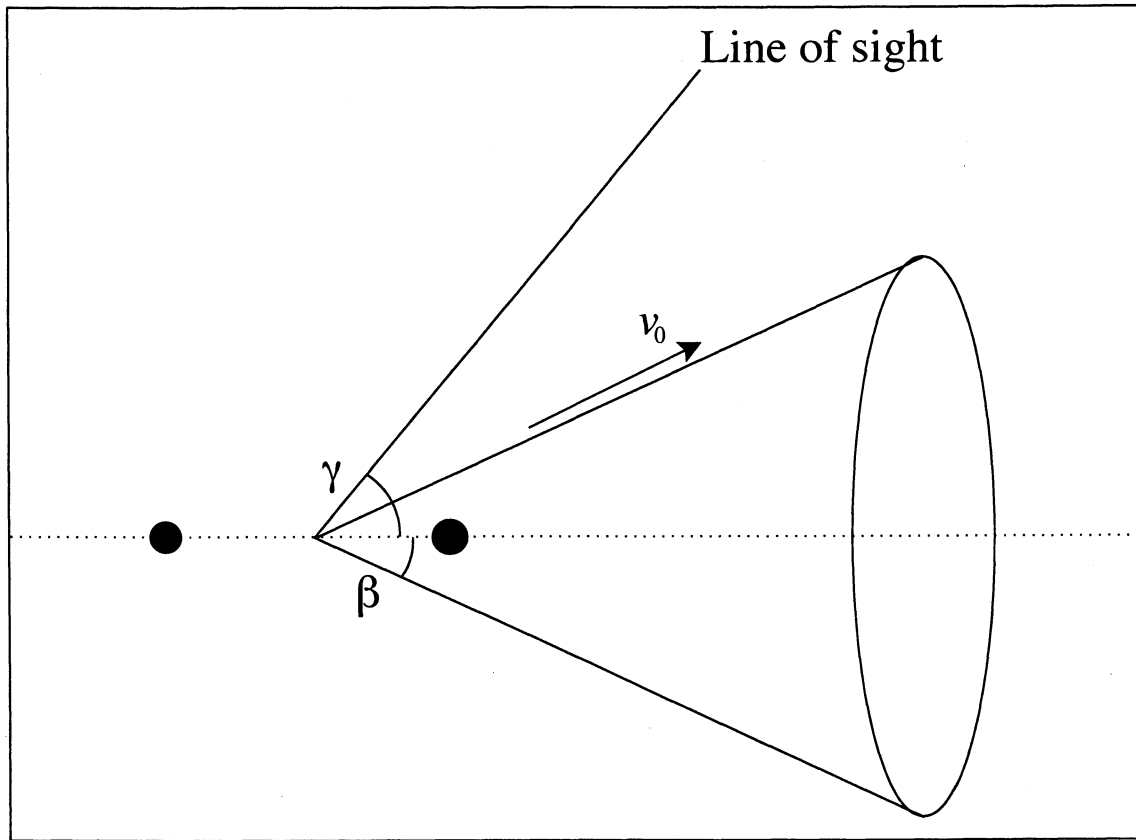
Fig. 16.— Geometrical model of the wind-wind collision in η Car. The solid circles represent the two stars. The cone (with opening half-angle β) represents the wind-wind interaction region (along which X-ray–emitting material is streaming at speed v_0). The viewing angle γ is the angle between the line of sight and the line of centers.
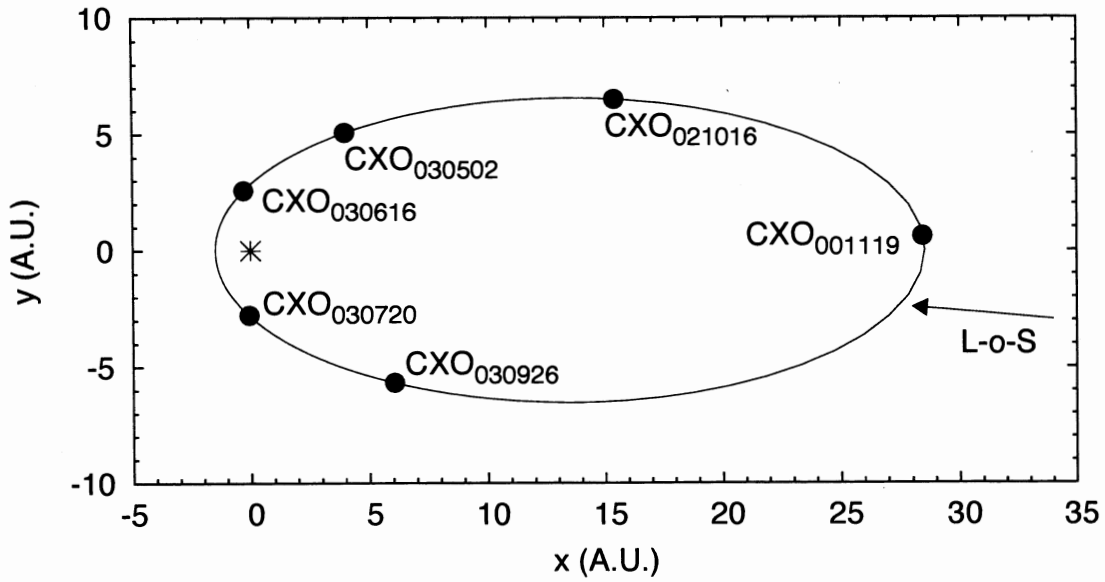
Fig. 17.— The orbit of η Car's companion plotted in the rest frame of the primary (marked with an asterisk at the origin). The positions of the companion at the times of the *Chandra* HETGS observations are marked with black circles. The arrow shows the line of sight (L-of-S) projected into the orbital plane. This orbit was plotted using the parameters in Table 6. The length scale of the orbit is set by assuming masses of $80M_\odot$ and $30M_\odot$ for the primary and the companion, respectively (Corcoran et al. 2001a).
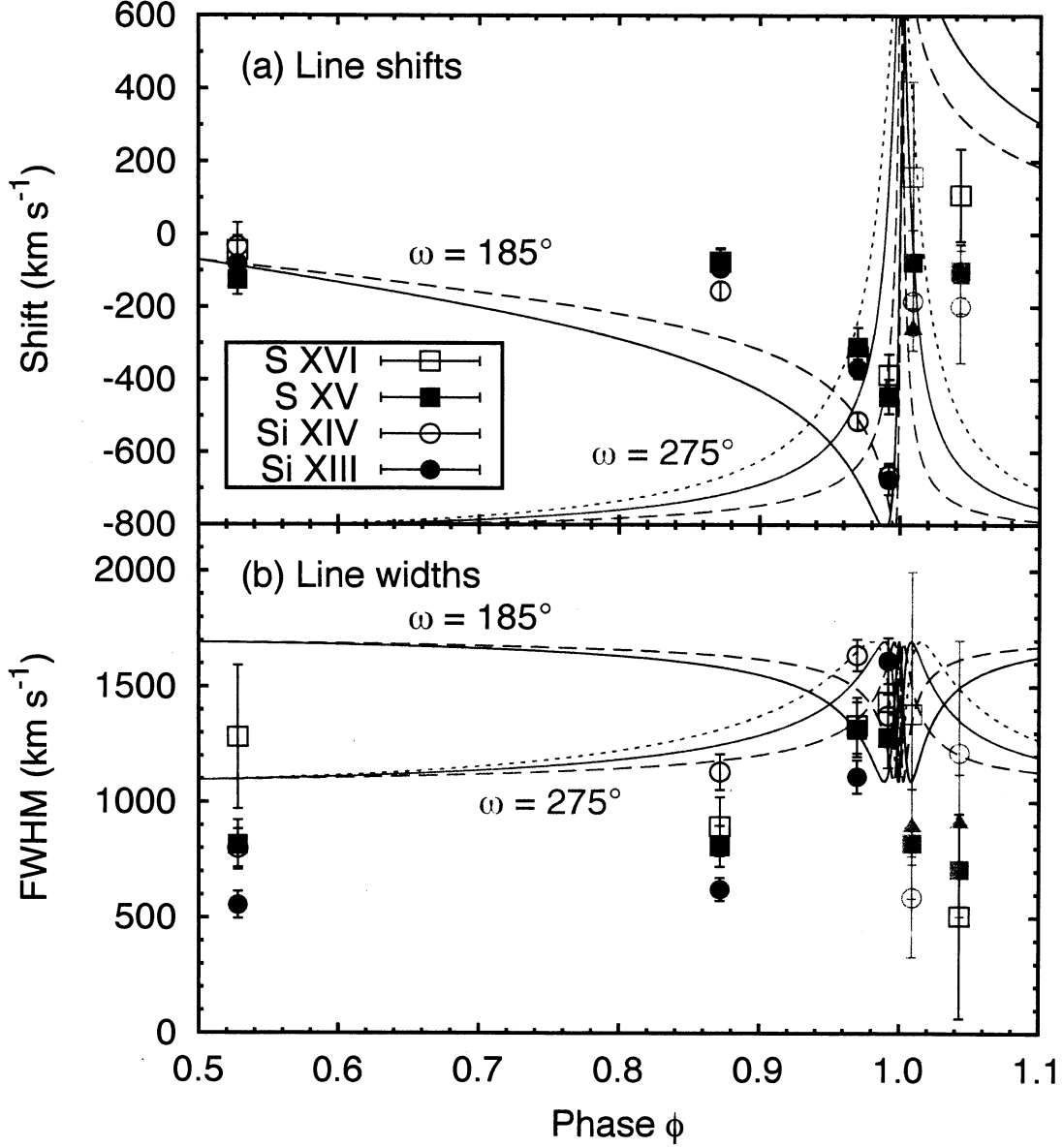
Fig. 18.— Comparison of the predictions of the simple geometrical model (§4) with the observed line shifts and widths. The solid red curves were generated from the orbital parameters in Table 6 ($i = 50°$, $\omega = 275°$, $e = 0.9$). The other red curves show the effect of varying the eccentricity: $e = 0.85$ (*short dashed*) and $e = 0.95$ (*long dashed*). The blue curves show the effect of adjusting ω to 185°, for two different eccentricities: $e = 0.9$ (*solid*) and $e = 0.95$ (*long dashed*). The gray datapoints are for lines contaminated by the CCE component (Hamaguchi et al. 2007).
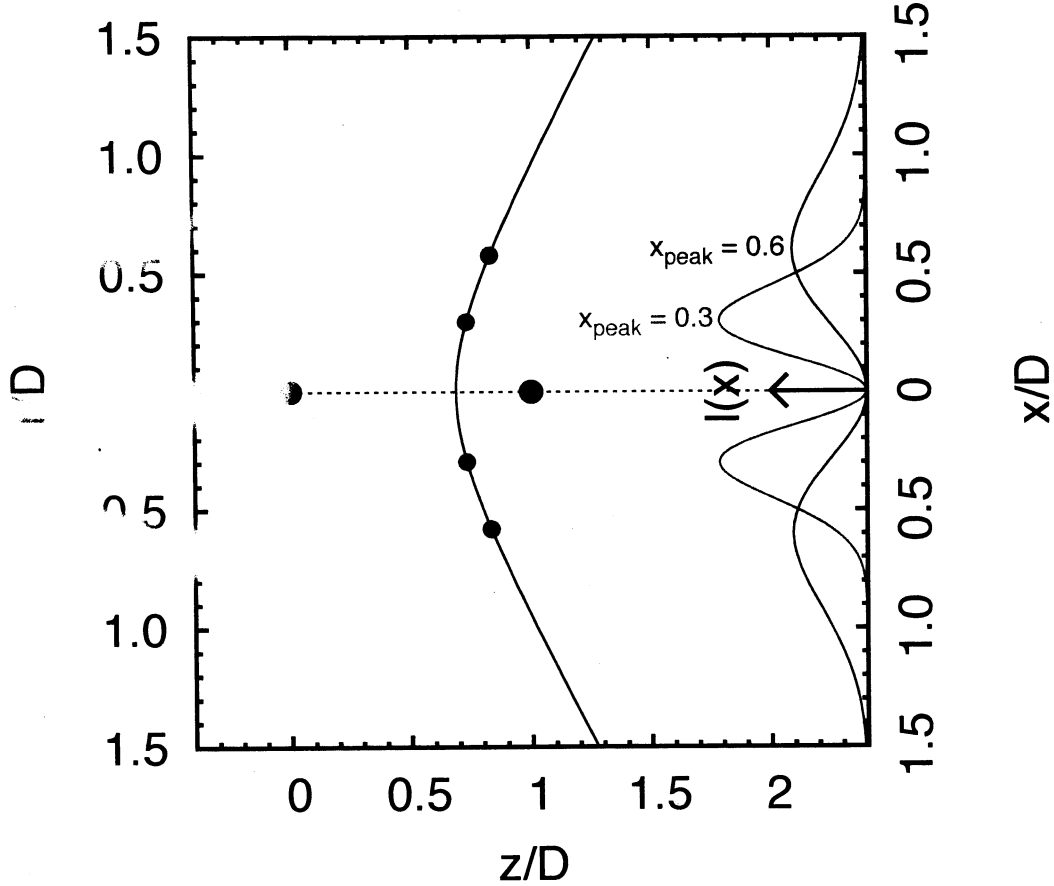
Fig. 19.— The shape of the wind-wind collision surface in η Car, calculated using the equations of Cantó et al. (1996). The two stars are shown by the black circles on the z axis: the primary is at the origin, and the companion is at (1,0). Distances are normalized to the stellar separation D. The curves to the right show $l(x)$ (see eq. [8]) plotted for two different values of x_{peak} (red: $x_{peak} = 0.3$; blue: $x_{peak} = 0.6$). Note that x is actually the distance measured along the wind-wind collision surface. The points at $x = 0.3$ and $x = 0.6$ are marked on the surface with the red and blue circles.
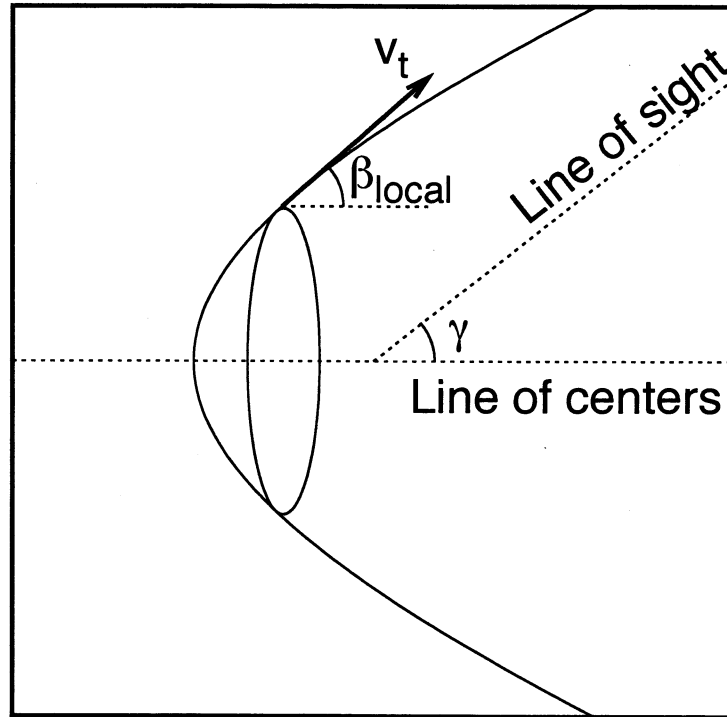
Fig. 20.— Diagram showing the geometry used in the line profile calculations. Each point along the wind-wind collision surface represents a ring of expanding material, comprising material flowing tangentially along the wind-wind collision surface at speed v_t. Locally, the flow velocity makes an angle β_{local} with the line of centers, while the line of sight makes an angle γ with the line of sight. Note that the curvature of the surface has been exaggerated for clarity.
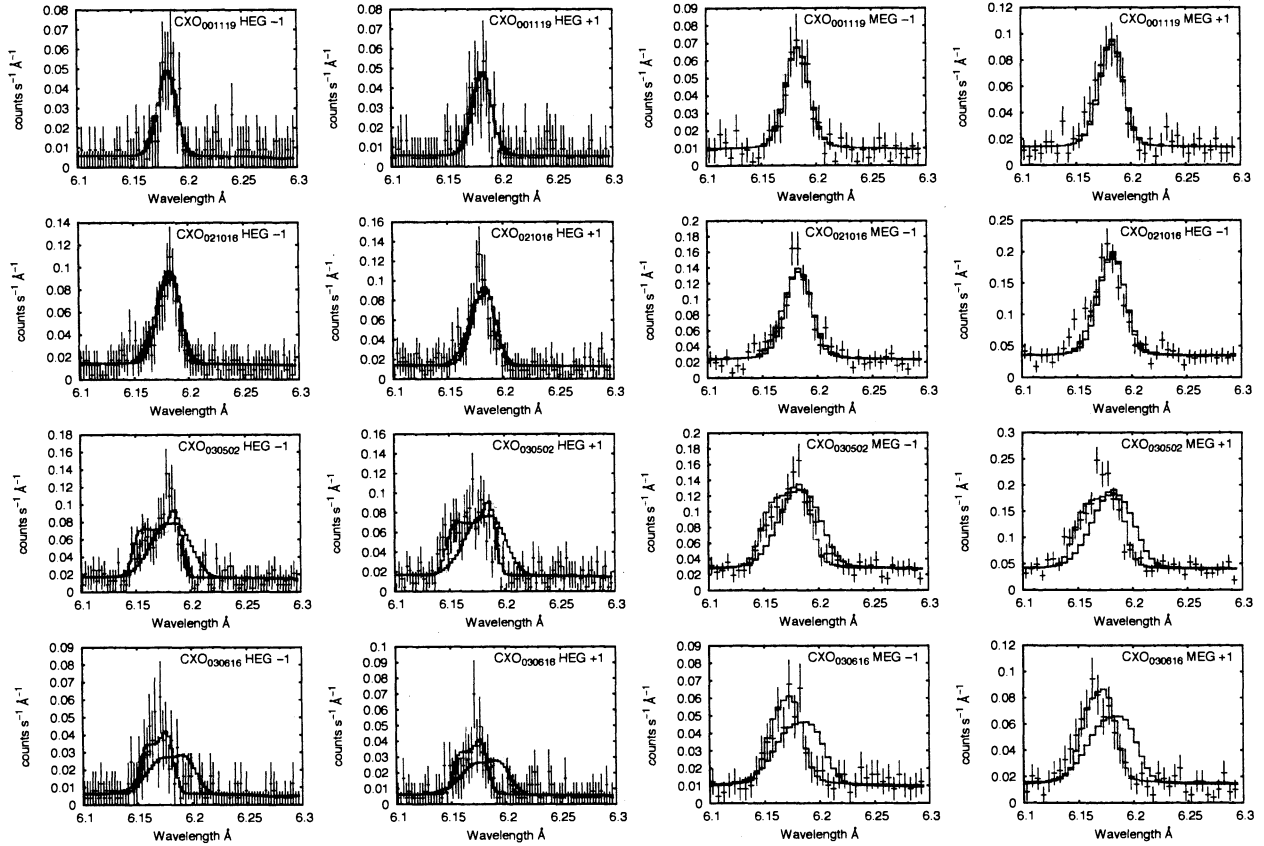
Fig. 21.— Comparison of our model profiles with the observed Si XIV Lyα lines, from CXO_{001119}, CXO_{021016}, CXO_{030502}, and CXO_{030616} (plotted from top to bottom). Each spectral order is plotted separately. The red curves show the profiles calculated with $\omega = 210°$, $i = 70°$, the green curves the profiles calculated with $\omega = 270°$, $i = 50°$, and the blue curves the profiles calculated with $\omega = 180°$, $i = 50°$.
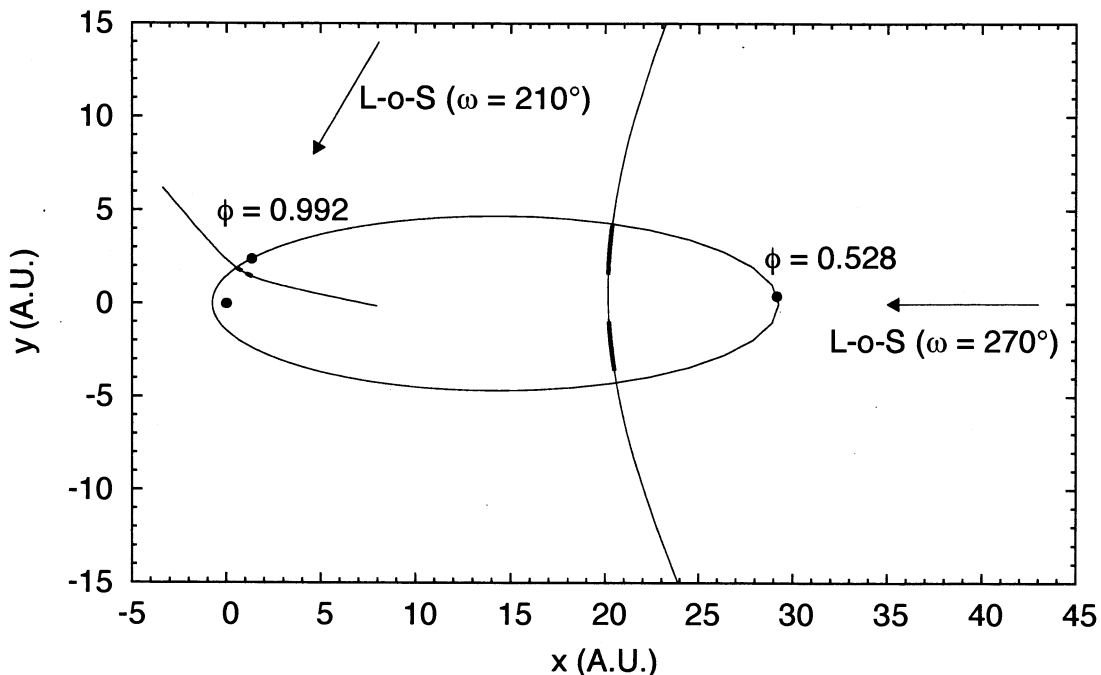
Fig. 22.— The orbit of η Car with the eccentricity ($e = 0.95$) from our line profile modeling. All other orbital parameters are the same as those used in Figure 17. The arrows show the lines of sight (L-of-S) projected into the orbital plane for two different values of the longitude of periastron – that obtained without including absorption in the model ($\omega = 210°$; see §5.2), and that obtained when the effects of absorption are included in the model ($\omega = 270°$; see §5.3). Also shown is a comparison of the stellar orientations and geometry of the contact discontinuity for two phases corresponding to observations CXO_{001119} ($\phi = 0.528$) and CXO_{030616} ($\phi = 0.992$). In each case the red interval shows the approximate x range where the line luminosity $l(x)$ (see eq. [8]) is greater than half its maximum value for the Si XIV line. We plot results for the version of the model which includes the effects of absorption (§5.3; lower part of Table 7). The extent of the S XVI emission region is similar to that of the Si XIV emission region.
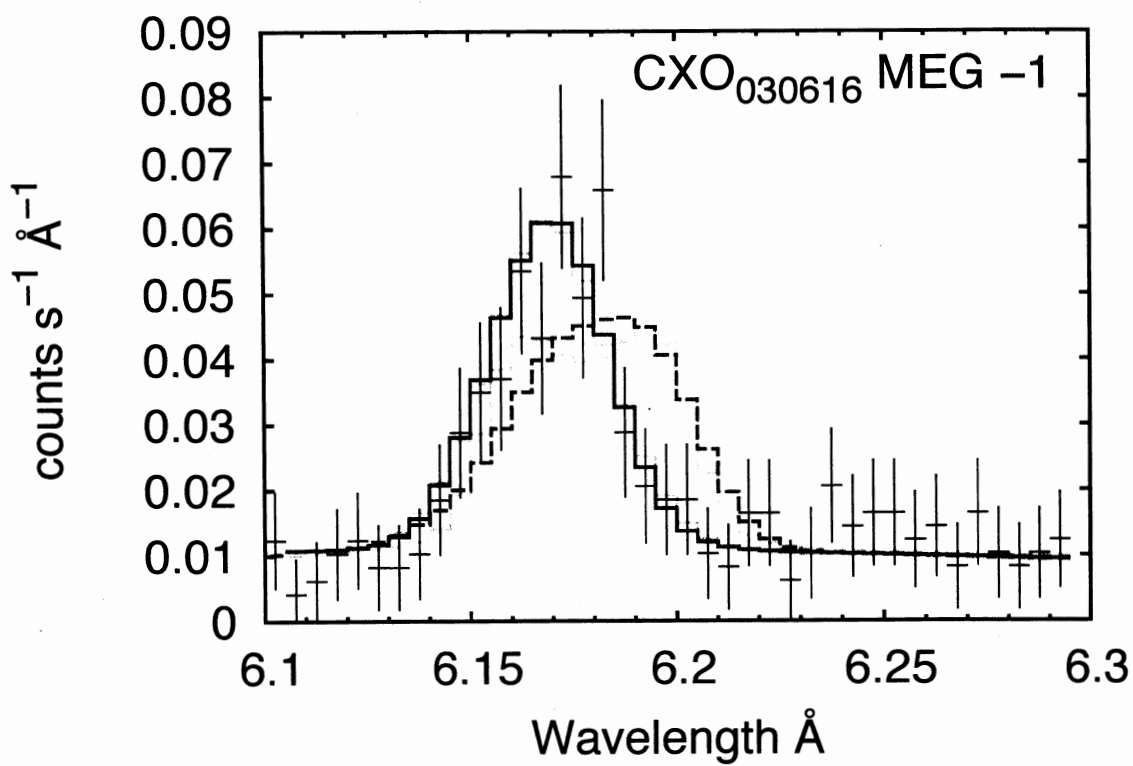
Fig. 23.— Model Si XIV profiles with (*solid*) and without (*dashed*) absorption, compared with the MEG −1 Si XIV line from CXO_{030616}. As in Figure 21, the green profiles were calculated with $\omega = 270°$, $i = 50°$, and the blue profiles with $\omega = 180°$, $i = 50°$.
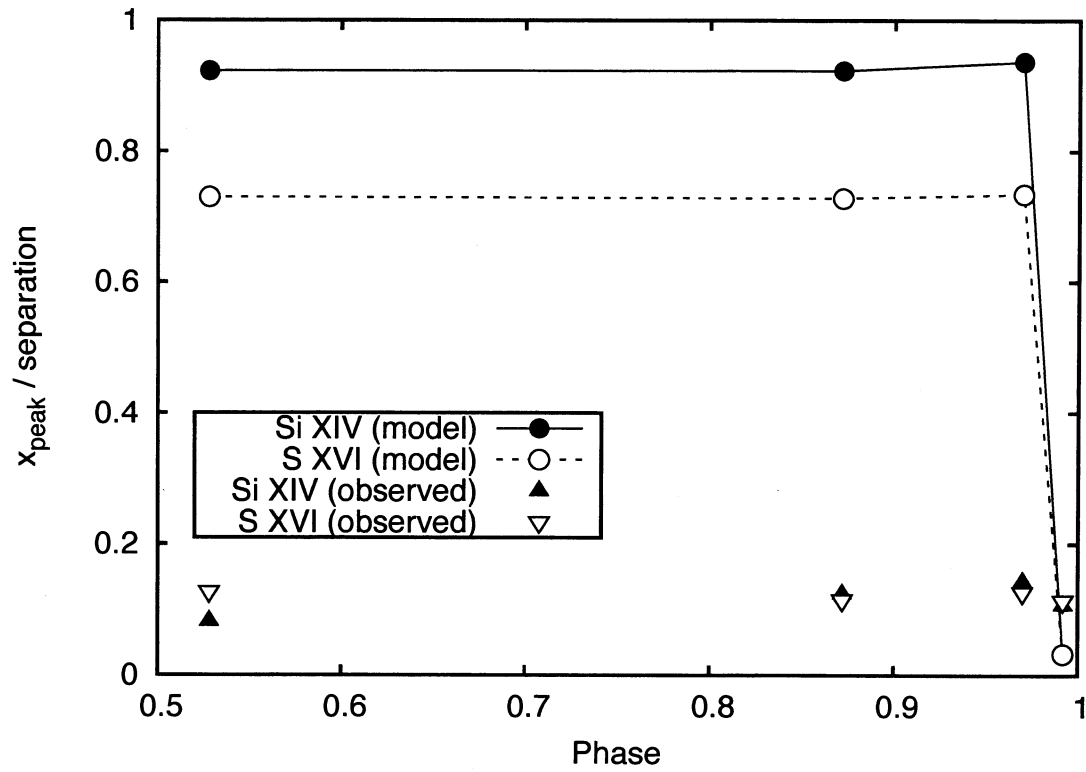
Fig. 24.— The values of x_{peak} measured from the observed Si XIV and S XVI line profiles (*triangles*), plotted alongside the values of x_{peak} expected from hydrodynamical simulations (*circles*). In all cases the values of x_{peak} have been normalized to the stellar separation.